NASA/TM—2012–216052

Development of a Fluid Structures Interaction Test Technique for Fabrics

Gregory G. Zilliac
James T. Heineck
Edward T. Schairer
Robert N. Mosher
Theodore J. Garbeff
Louise A. Walker

Ames Research Center, Moffett Field, California

September 2012

NASA STI Program ... in Profile

Since its founding, NASA has been dedicated to the advancement of aeronautics and space science. The NASA scientific and technical information (STI) program plays a key part in helping NASA maintain this important role.

The NASA STI program operates under the auspices of the Agency Chief Information Officer. It collects, organizes, provides for archiving, and disseminates NASA's STI. The NASA STI program provides access to the NASA Aeronautics and Space Database and its public interface, the NASA Technical Reports Server, thus providing one of the largest collections of aeronautical and space science STI in the world. Results are published in both non-NASA channels and by NASA in the NASA STI Report Series, which includes the following report types:

- TECHNICAL PUBLICATION. Reports of completed research or a major significant phase of research that present the results of NASA Programs and include extensive data or theoretical analysis. Includes compilations of significant scientific and technical data and information deemed to be of continuing reference value. NASA counterpart of peer-reviewed formal professional papers but has less stringent limitations on manuscript length and extent of graphic presentations.

- TECHNICAL MEMORANDUM. Scientific and technical findings that are preliminary or of specialized interest, e.g., quick release reports, working papers, and bibliographies that contain minimal annotation. Does not contain extensive analysis.

- CONTRACTOR REPORT. Scientific and technical findings by NASA-sponsored contractors and grantees.

- CONFERENCE PUBLICATION. Collected papers from scientific and technical conferences, symposia, seminars, or other meetings sponsored or co-sponsored by NASA.

- SPECIAL PUBLICATION. Scientific, technical, or historical information from NASA programs, projects, and missions, often concerned with subjects having substantial public interest.

- TECHNICAL TRANSLATION. English-language translations of foreign scientific and technical material pertinent to NASA's mission.

Specialized services also include organizing and publishing research results, distributing specialized research announcements and feeds, providing information desk and personal search support, and enabling data exchange services.

For more information about the NASA STI program, see the following:

- Access the NASA STI program home page at http://www.sti.nasa.gov

- E-mail your question to help@sti.nasa.gov

- Fax your question to the NASA STI Information Desk at 443-757-5803

- Phone the NASA STI Information Desk at 443-757-5802

- Write to:
  STI Information Desk
  NASA Center for AeroSpace Information
  7115 Standard Drive
  Hanover, MD 21076-1320

NASA/TM—2012–216052

Development of a Fluid Structures Interaction Test Technique for Fabrics

Gregory G. Zilliac
James T. Heineck
Edward T. Schairer
Robert N. Mosher
Theodore J. Garbeff
Louise A. Walker

Ames Research Center, Moffett Field, California

National Aeronautics and
Space Administration

Ames Research Center
Moffett Field, CA 94035-1000

September 2012

Acknowledgments

We would like to acknowledge the support of the NASA Hypersonics program for this work. Specifically, we would like to acknowledge the contributions of Scott Murman, David Kinney (ARC) and Charles Player (LaRC) in the conceptualization and planning stages of this experiment.

Development of a Fluid Structures Interaction Test Technique for Fabrics

Gregory G. Zilliac
James T. Heineck
Edward T. Schairer
Robert N. Mosher
Theodore J. Garbeff
Louise A. Walker

Ames Research Center

SUMMARY

Application of fluid structures interaction (FSI) computational techniques to configurations of interest to the entry, descent and landing (EDL) community is limited by two factors – limited characterization of the material properties for fabrics of interest and insufficient experimental data to validate the FSI codes. Recently ILC Dover Inc. performed standard tests to characterize the static stress-strain response of four candidate fabrics for use in EDL applications. The objective of the tests described here is to address the need for a FSI dataset for CFD validation purposes. To reach this objective, the structural response of fabrics was measured in a very simple aerodynamic environment with well controlled boundary conditions. Two test series were undertaken. The first series covered a range of tunnel conditions and the second focused on conditions that resulted in fabric panel buckling.

INTRODUCTION

Three configurations (i.e. ballutes, tension cones and stacked toroids) are currently under consideration by the NASA EDL program for missions that require landing high mass payloads on planets with thin atmospheres. FSI computations of some of the configurations of interest have been completed with various degrees of success. Shown in figure 1 from reference 1 is a result computed using the NSCART-GT Navier Stokes code coupled with the LS-DYNA transient dynamic finite element code that illustrates some of the challenges involved in the computation of a tension-cone decelerator. In particular, the wrinkling in the fabric under aerodynamic load is problematic in several respects including the obvious challenges of generating a grid adjacent to the fabric surface.

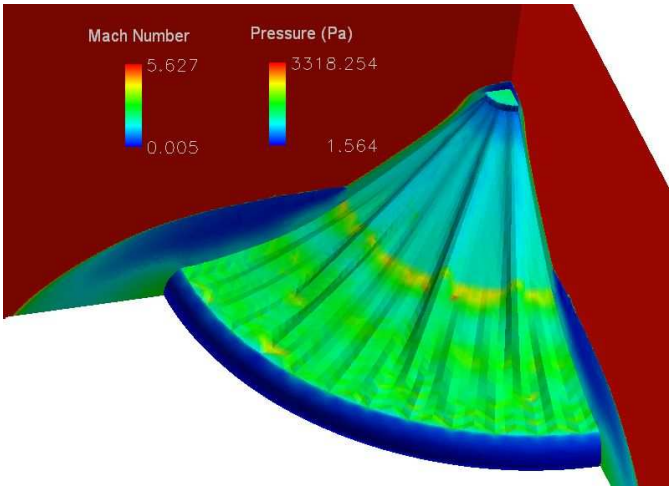

Figure 1. FSI simulation of a tension-cone decelerator (from Ref. 1 with permission).

In addition, to the wrinkling that results from highly dissimilar components of strain, (i.e. the strain along a ray emanating from the apex is significantly greater than that in the circumferential direction) the basic response of the fabric in an aerodynamic environment is likely to be substantially different from that measured in standard fabric material properties tests because the loading is different (aerodynamic loads are directed normal to the surface). In addition, woven fabrics behave differently than isotropic materials in that they have a degree of porosity, creep while loaded and apparently have a memory (i.e. some fabrics have been observed to remain deformed after they are unloaded and then they slowly return to their original state after a period of hours to days).

The behavior of loaded fabrics has been explored in several studies. Presented in reference 2 are the results of four different test techniques performed on five coated fabrics to characterize the stress-strain and shear stress-strain behavior. The testing included using a trellis frame to measure the in-plane shear stress response to shear strain, a bias extension test, an uni-axial pull test and a cylindrical biaxial test. The results showed a significant degree of nonlinearity and hysteresis in virtually all of the tests performed.

In reference 3, thin square membranes subjected to symmetrical corner loading were tested and modeled. Photogrammetry was used to measure the membrane deformation. The modeled and measured results agreed reasonably well in terms of the overall wrinkling amplitude, extent and frequency although the test results were not found to be very repeatable. Some of the details of the wrinkles were not captured by the modeling. It was determined that the wrinkles in the membrane formed along lines in the direction of the major principle stress.

Shown in reference 4 are the results of a finite element calculation of a rectangular Kapton polyimide membrane subjected to shear. The modeled wrinkling pattern is similar to that visualized in an actual membrane but no quantitative comparisons were presented.

Woven fabric shear deformation test techniques were surveyed in reference 5. The test methodologies of seven international research organizations were compared on three identical woven fabrics. It was found that the details of the various trellis frame designs lead to significant differences in the measured shear force versus shear angle trends. The data set collapse was improved after the data were corrected for differences in the frame geometry through use of an “amplification factor.” Furthermore, it was found that the data repeatability could be greatly improved through mechanical conditioning (i.e. shearing the fabric in the frame several times before starting the test).

The importance of proper alignment of fabric test samples in trellis frame shear tests was pointed out in reference 6. In this reference, the load–displacement traces of the bias extension tests were compared with those measured using a modified trellis-frame. It was found that if the poly-propylene and glass-fiber fabric was properly aligned in the frame and the shearing velocity was accounted for, both tests gave similar shearing loads.

The references cited above bring to light certain challenges in measuring the basic material properties required to model the response of fabrics and membranes to static loads. In EDL applications the complexity is even greater because of the effects of fabric porosity, aerodynamic heating and dynamic loads. The current experiment represents a first attempt to incorporate some of these factors. It is recognized that the results presented here are imperfect and additional measurement technique refinement and testing will be required in order to develop a comprehensive dataset suitable for FSI validation purposes.

TEST DESCRIPTION

The overall approach to the FSI validation experiment is to apply known structural and aerodynamic loads to a fabric panel and measure the corresponding deformation of the panel and the flow field adjacent to the deformed fabric surface. The deformation of the panel is measured using a two-camera photogrammetry system and the flow field is measured using Particle Image Velocimetry (PIV).

Fabrics Tested

The fabrics supplied by ILC Dover Inc for use in this study are highlighted in Table 1. During the first test entry, which is the subject of this report, only the F-111 Nylon and ST11-4600 Kevlar were tested.

Table 1. Fabrics provided by ILC Dover Inc. for testing.

	Fiber Density *(g/cm³)*	**Denier**	**Yarn Density** *(yarns/inch)*	**Coating Add-On** *(oz/yd²)*	**Mean Fabric Density** *(g/cm³)*
Uncoated Nylon (F-111)	1.14	30	126 x 132	NA	**1.1534**
Silicone Coated Nomex (Style HT1)	1.38	200	101 x 92	3.5	**1.1456**
Silicone Coated Kevlar (ST11-4545)	1.44	200	40 x 40	5.9	**1.1099**
Silicone Coated Kevlar (ST11-4600)	1.44	840	26 x 26	4.4	**1.0730**

Selected material properties of these fabrics have been measured by ILC Dover (see reference 2) and the fabrics from the same production run are used in the current study.

Wind Tunnel

Shown in figure 2 is the 14x14 in transonic wind tunnel, located in test cell 3 in the Fluid Mechanics Laboratory at NASA Ames, that was used in the testing. This is an indraft wind tunnel that has a Mach number range of 0.13 to 0.58 and the static pressure in the test section is up to 2.5 psi less than atmospheric depending on the Mach number. Mach number is set by adjusting the height of a choked nozzle between the test section and the diffuser. The nozzle prevents disturbances from the diffuser from propagating upstream into the test section. The tunnel was instrumented with a Setra Inc. Datum 2000 differential pressure transducer to measure the free stream dynamic pressure and Omega Inc. model PX409-005CG5V pressure transducers that were used to measure the test section and plenum static pressure levels.

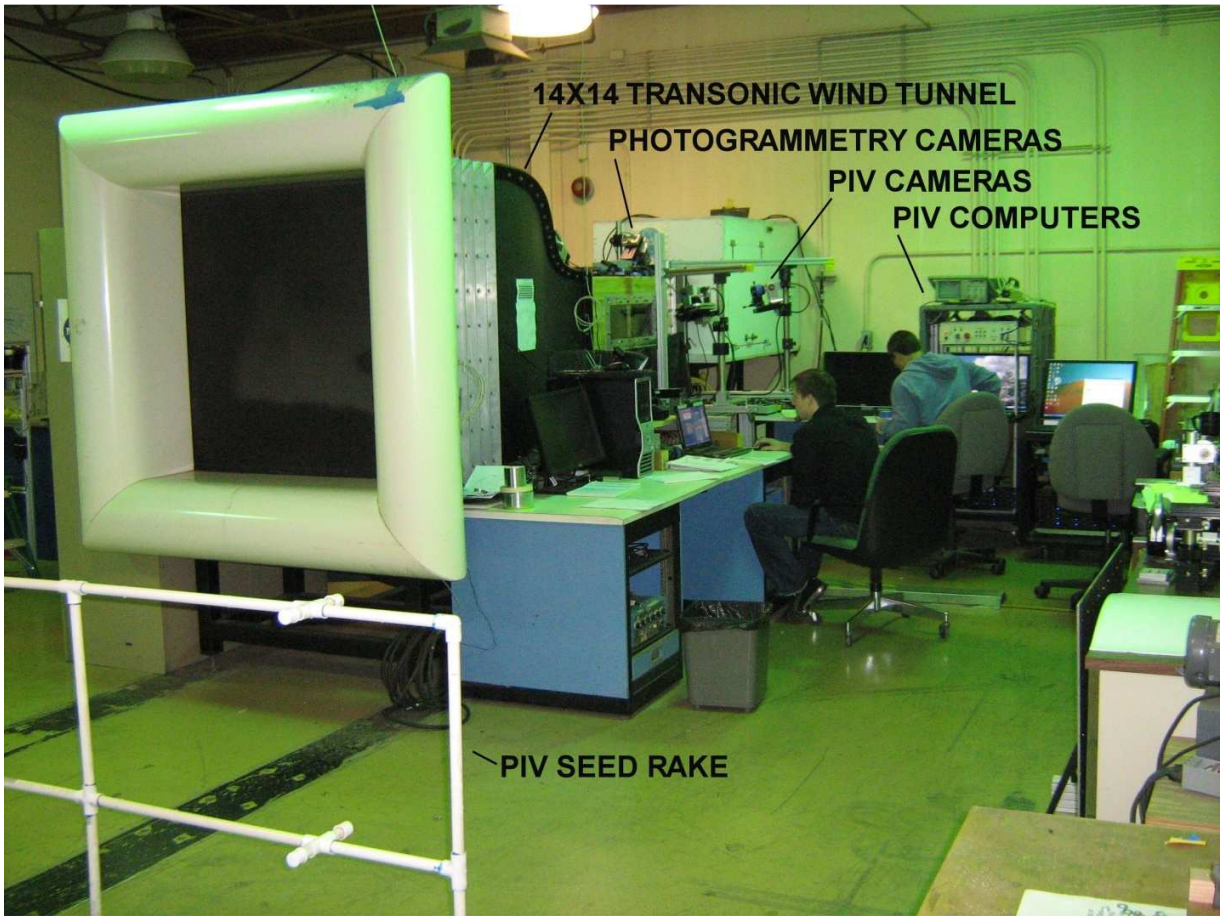

Figure 2. The FML 14×14 inch transonic tunnel and associated instrumentation.

Test Hardware

The fabric test panels were installed in a custom designed stainless steel trellis frame (see figures 3-6) using specialty tooling that was developed to maintain the orientation of the fabric panel while the side clamps were installed. Fabric installation was performed on a bench while the trellis frame was held in the square configuration. After the fabric panel installation process was completed, the initial fabric panel tension was measured using a Newman ST tensionometer and then the trellis frame assembly was installed in the tunnel floor followed by adjustment of the jack screws to set the desired frame elongation. Plates with cutouts that matched each elongated frame configuration were then bolted and sealed in place in such a manner that the undeformed surface of the fabric was flush with the floor of the test section and there were no significant steps or gaps between the fabric panel and the rest of the tunnel floor. The fabric was installed so that either the warp or fill direction was aligned with the free-stream flow direction. Some tests were also performed with fabric oriented at 45 degrees to the frame axis.

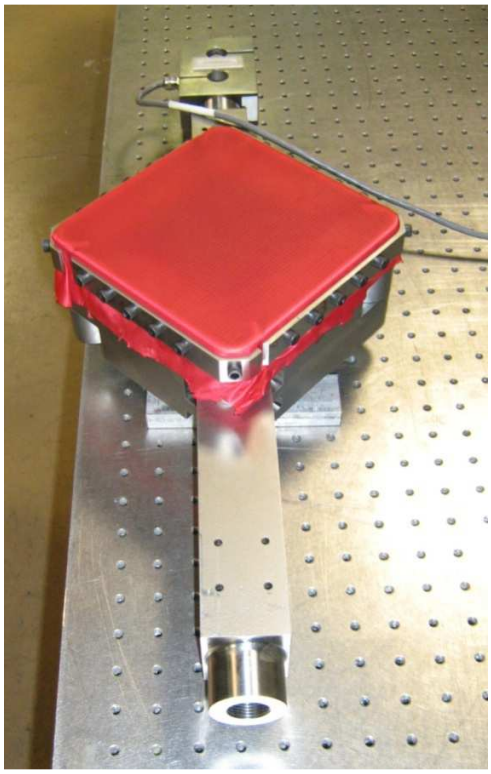

Figure 3. F-111 Nylon fabric installed in trellis frame.

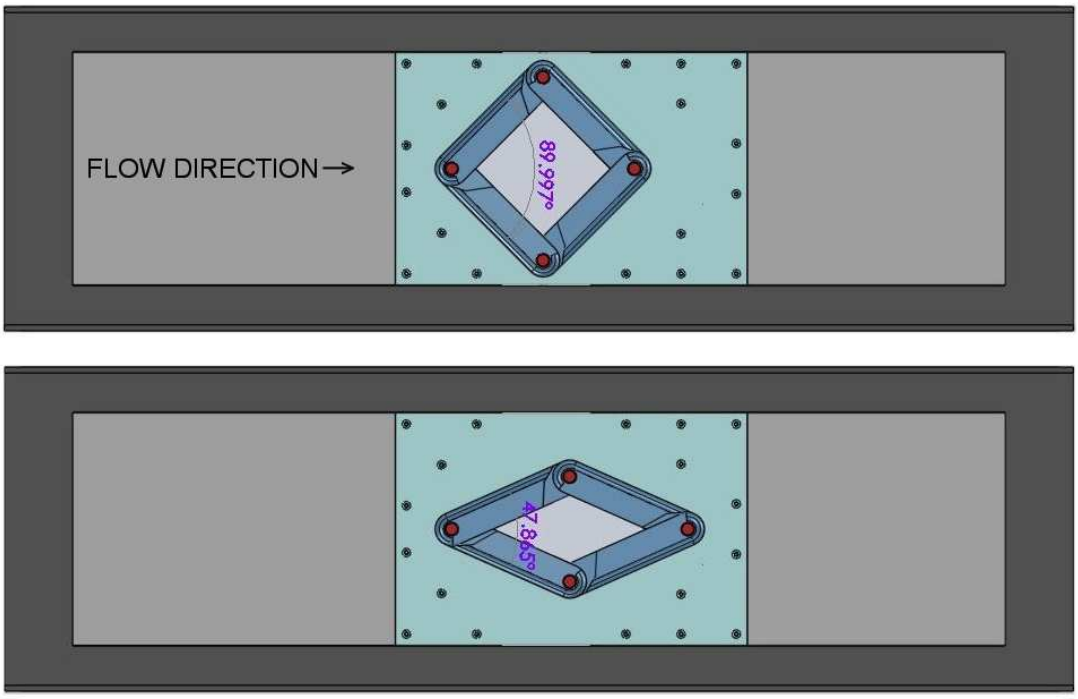

Figure 4. CAD model showing trellis frame range of extension.

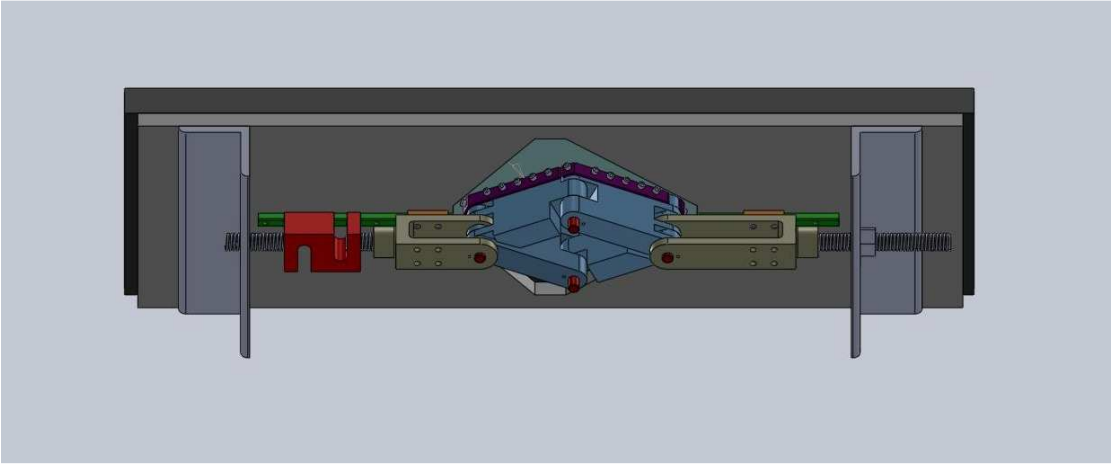

Figure 5. CAD model of trellis frame integrated into a wind tunnel wall (underside).

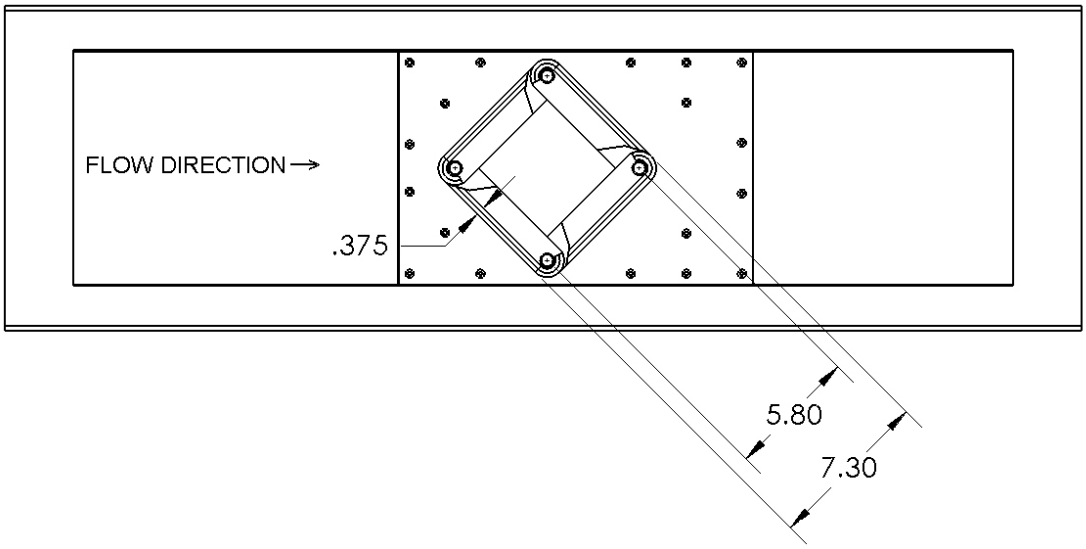

Figure 6. Fabric frame dimensions (in inches)

The dimensions of the trellis frame are shown in Figure 6. The installed fabric rests on the edges of the frame which have a radius of 0.1875 inches in order to limit stress concentrations in the fabric. The unsupported portion of the fabric panel is 6.925 × 6.925 inches. As the trellis was elongated, the upstream corner remained at the same stream-wise position, the downstream corner moved downstream, and the outboard corners moved toward the tunnel centerline (Figure 4).

The trellis frame is capable of applying axial loads up to 20,000 lbs with axial elongations of up to a 2.5 inches. This range exceeded the axial tension and shear levels that were studied in the ILC Dover static tests. The applied tension in the fabric panel was measured by an Omega LC 101-10K load cell. It should be noted that the 1.5 inch by 4 inch (width x height) stainless steel frame is very stiff in order to produce well know boundary conditions. The high-load capability was designed into the apparatus in order to cover a wide range of fabrics types (from thin stretchy Nylon to thick Kevlar). It was also deemed important to have the capability to fail the fabrics in tension in order to provide useful information for decellerator designers because the ultimate strength of the fabrics under aerodynamic load are currently unknown.

A plenum was fabricated to enclose the trellis frame assembly thus permitting the back side of the fabric panel to be pressurized up to 3 psi above the test section free-stream static pressure thereby creating a substantial pressure differential across the fabric (see Figure 7). The plenum pressure is set by a Proportionair QB-3 pressure regulator that allows air to be drawn into the plenum from the ambient environment. For highly porous fabrics, (e.g. F-111 Nylon) an auxillary compressor was used to increase the pleunum pressure level. The primary test series consisted of plenum pressure sweeps (i.e. fabric Δp loading) on samples that were pre-elongated (stressed) to pre-determined elongations by the jack screw.

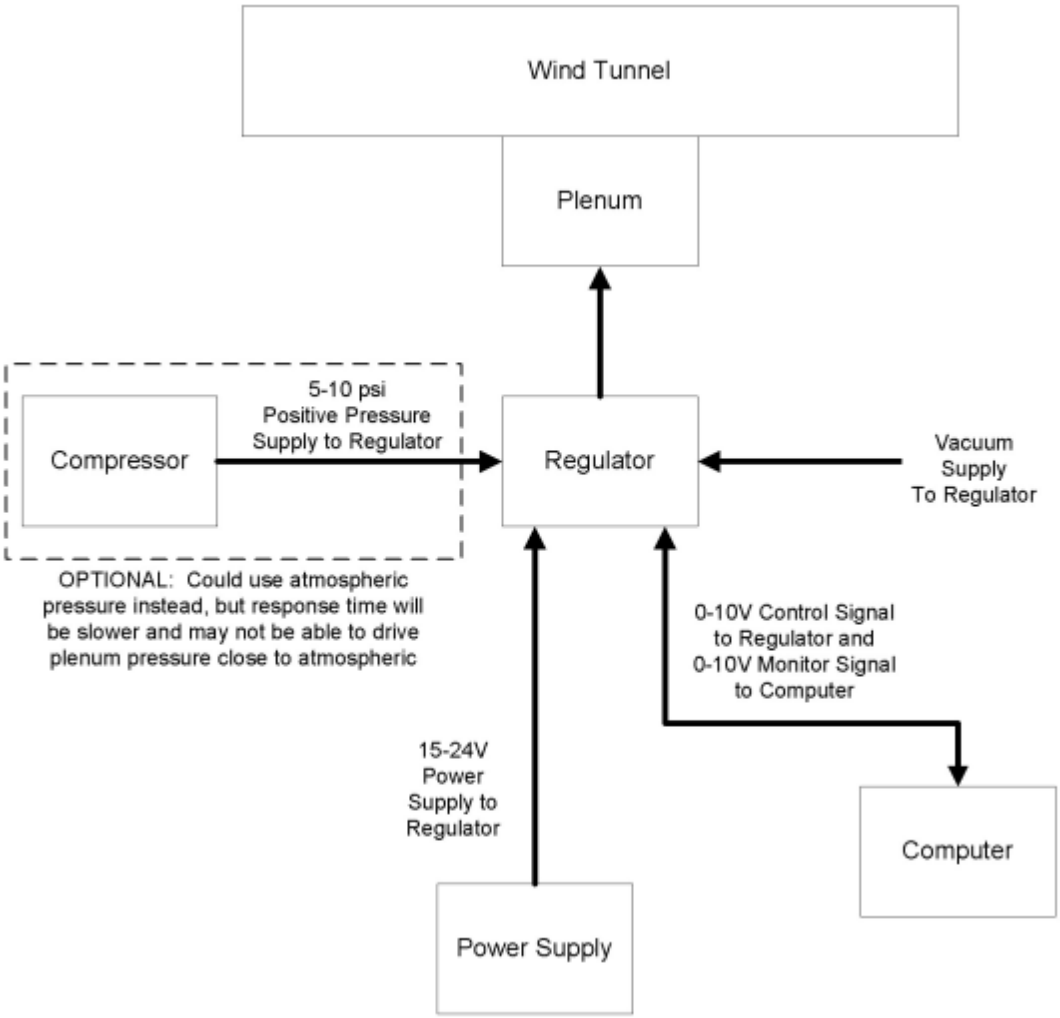

Figure 7. Diagram of the plenum pressure control system.

Typically, the fabric loading was a combination of aerodynamic loading and tension applied by the frame depending on the objective of the particular measurement. Three adjustments can be made to establish a FSI combined load. The tensioning screw can be adjusted to stress the fabric with forces up to 20,000 lbf possible. The static pressure on the back side of the fabric can be adjusted over a range of nearly 3 psi (depending on the tunnel Mach number) and the pressure distribution on the flow side of the fabric can be adjusted within certain limits to establish a pressure gradient over the surface. In addition, the initial fabric tension established during fabric installation can be adjusted (and is measured using a tensionometer). Through adjustment of these four variables, it is possible to expose the fabric to loading conditions similar to that experienced in a range of EDL applications thereby creating a validation dataset that will be relevant to EDL. This is an important aspect of the

design of the experiment because of the known highly nonlinear behavior of the fabrics.

Tests were performed with and without pressure gradient effects. A pressure gradient was created by a 2 inch high by 26.5 inch long filleted circular arc insert placed on the opposing (upper) wind tunnel wall (as shown schematically in figure 8). The radius of the circular arc is 37.5 inches. Also shown in Figures 8 is a Navier-Stokes prediction of the far-wall pressure variation created on the fabric panel by a similar insert (note that computed and actual dimensions and Mach number differ slightly). Shown in the figure is the approximate stream-wise position of the fabric test sample (unstretched and fully stretched) relative to the insert. Circular fillets of 10 inch radius on the upstream and downstream ends of the insert prevented flow separation near the junctures between the tunnel wall and the circular arc. Combining the stream-wise pressure variation arising from the circular arc with the pressure loading due to the difference between the free-stream static and plenum pressures results in a fabric loading that is representative in many respects to that experienced by a tension cone decelerator (see ref 1). During the wind tunnel test, the nominal free-stream Mach number was 0.46 which corresponds to a free stream velocity of 500 ft/sec. Under these conditions, the measured tunnel free stream static pressure is 2.0 psi below atmospheric.

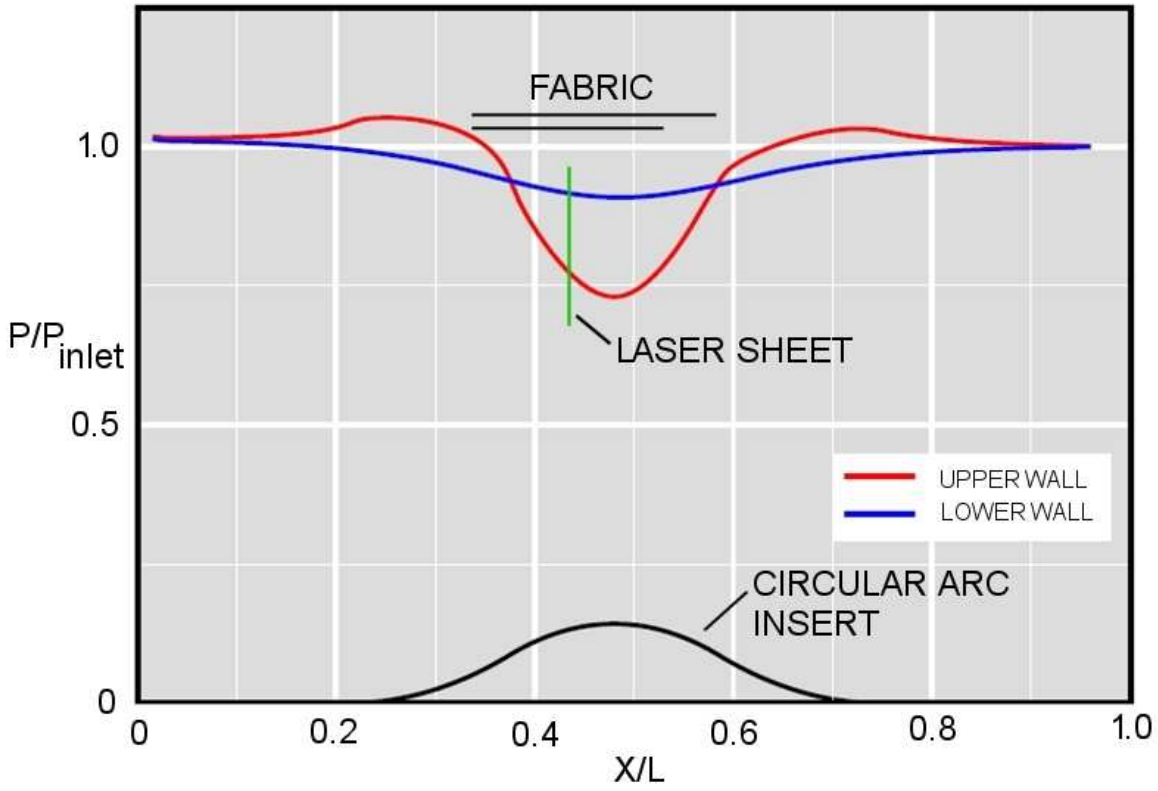

Figure 8. Wall pressure distribution for 2-in high filleted circular arc at M=0.58.

PIV System

Stereo PIV (SPIV) was used to measure the flowfield in a vertical cross-stream plane at approximately the mid point of the fabric panel at zero elongation.

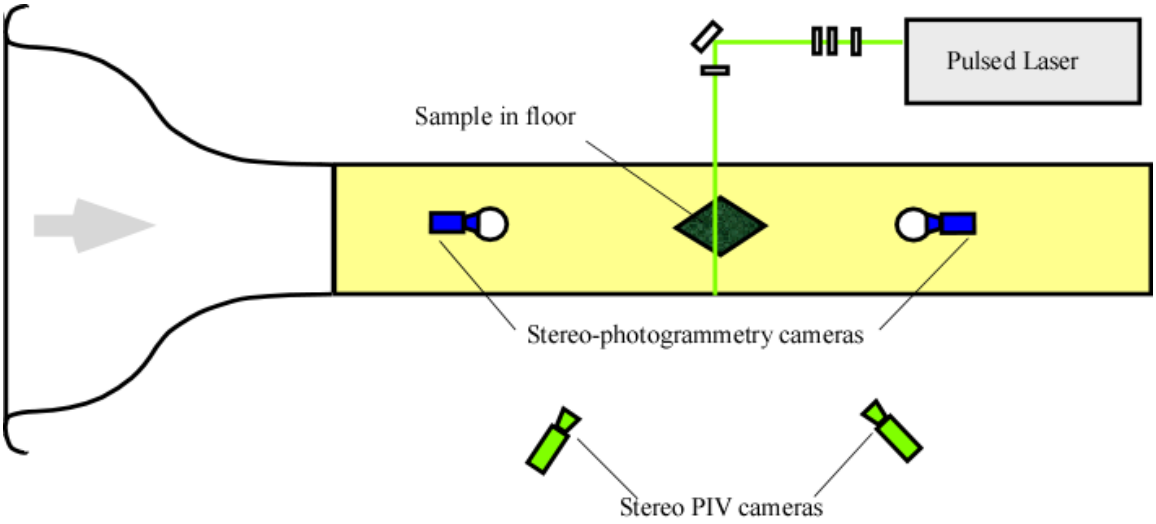

Figure 9. Plan-view illustration of the imaging systems for photogrammetry and SPIV.

The system consisted of a dual-cavity Nd:YAG pulsed laser, operating at 350 millijoules (mJ) per pulse and two frame-straddling cameras with sensors of 2048 x 2048 pixels. A laser sheet was projected across the tunnel in a vertical plane and the cameras were on the opposite side of the tunnel upstream and downstream of the laser plane (Figure 9). The lower edge of the laser sheet was adjusted to barely grazed the crest of the deformed model at each condition. Thus, the height of the lower edge of the laser sheet provided an estimate of the maximum model displacement at the laser station that was independent from the photogrammetry measurements. The images were stored after the photogrammetry data were acquired on a separate RAID system. The PIV software for both data acquisition and reduction was LaVision's DaVis 8. The images were processed using a multi-pass method with the final pass setting of 32x32 pixels with 25% overlap. No less than 300 instances were acquired for each condition, with a simple average of all the instantaneous velocity fields presented here.

FSI Photogrammetry

The displacement of the model was measured by stereo photogrammetry. The model was imaged by two synchronized cameras located behind 3.5-in dia circular windows in the top wall on the centerline of the test section, equidistant upstream and downstream of the model. The location of the windows (and thus the cameras) were constrained by geometry and had to be located upstream and downstream of the circular-arc insert. This separation resulted in more oblique viewing angles of the model (about 60 degrees from the surface normal) and a larger convergence angle between the camera axes (about 120 degrees) than what is optimal (usually about 90 degrees). The high-resolution cameras (2048 x 2048 pixels, 7.4 µm pitch) were operated at 0.5 Hz. Because of the very oblique viewing angles of the model, the camera lenses (50 mm) were mounted independently from the camera bodies, and the angles of the camera bodies were adjusted to the Scheimpflug angle, resulting in sharp edge-to-edge focus of the model. The model was illuminated through the PIV window on the port side of the test section using two pulsed Xenon flash lamps, one upstream and one downstream, with a duration of 15 microseconds. The short duration prevented image blur. The images were streamed to a RAID and saved as individual TIFF images. The images were captured during the condition changes and for several seconds when conditions were set.

The cameras were calibrated before the model was installed by imaging a rectangular plate that fit in the model cut-out in the floor of the test section. The calibration plate included a rectangular array of targets (Fig. 10) and was supported by a linear translation stage that allowed precise displacements in the direction normal to the plate surface. The plate was imaged by both cameras over a range of plate displacements spanning the expected out-of-plane displacements of the model. The targets were located in all images, and a best fit of the Direct Linear Transformation (DLT), which is an approximation of the collinearity condition of photogrammetry, was computed for each camera. Each DLT provides a transformation between object-space (*x, y, z*) and image-plane (*X, Y*) coordinates (Ref. 7):

$$X = \frac{L_1 x + L_2 y + L_3 z + L_4}{L_9 x + L_{10} y + L_{11} z + 1}$$

$$Y = \frac{L_5 x + L_6 y + L_7 z + L_8}{L_9 x + L_{10} y + L_{11} z + 1} \qquad \text{(Eq. 1)}$$

When image-plane coordinates for the same point are available in the images of two cameras, the corresponding object-space coordinates are computed by solving the linear least-squares problem:

$$\begin{bmatrix} X^A L_9^A - L_1^A & X^A L_{10}^A - L_2^A & X^A L_{11}^A - L_3^A \\ Y^A L_9^A - L_5^A & Y^A L_{10}^A - L_6^A & Y^A L_{11}^A - L_7^A \\ X^B L_9^B - L_1^B & X^B L_{10}^B - L_2^B & X^B L_{11}^B - L_3^B \\ Y^B L_9^B - L_5^B & Y^B L_{10}^B - L_6^B & Y^B L_{11}^B - L_7^B \end{bmatrix} \times \begin{bmatrix} x \\ y \\ z \end{bmatrix} = \begin{bmatrix} L_4^A - X^A \\ L_8^A - Y^A \\ L_4^B - X^B \\ L_8^B - Y^B \end{bmatrix} \qquad \text{(Eq. 2)}$$

where superscripts A and B refer to images A and B, respectively.

Data analysis began by defining a planar, rectangular interrogation grid in object space and, with Eq. (1), projecting it into images from both cameras where the model was undeformed (Fig. 11). The grid was positioned to coincide with the undeformed surface of the model. The most critical step of data reduction was to assure that each node of the interrogation grid corresponds to the same physical point on the model in the images of both cameras. This was accomplished by cross-correlating image-data from each camera in a small (64 x 64 pixel) interrogation window centered on each node of the grid. Differences in perspective between the images, if left uncorrected, would overwhelm the cross-correlation function with noise. Therefore, both images were first dewarped to minimize perspective differences. The B-to-A cross correlation of the dewarped images at each node yielded a correction to the node position in image B so that the corrected position in image B corresponded to the same physical point as in image A.

After correspondence of nodes was established in the first images, where the model was not deformed, each node was tracked through the sequence of images from each camera independently of the other camera. The displacement of each node from one image to the next was determined by cross-correlating intensity data within an interrogation window centered on the node from the current and next image. Thus the surface grid conformed to the shape of the model as the model deformed. This procedure requires that the imaging rate be high enough that there are no abrupt changes in model shape between successive images. This was true in the present test except in rare cases when the plenum pressure changed very quickly. After image-plane coordinates of each node were computed for both cameras at each sequence, the object-space coordinates of the nodes were computed from Eq. (2).

The data-reduction procedure was the same as that used to measure the deformation of a tension-cone decelerator (Ref. 8) in a subsonic wind tunnel and the recession of ablation test articles

in arcjets (Ref. 9). An important requirement is that the approximate shape of the model must be known at least one condition. This is necessary so that a surface grid can be defined that conforms closely enough to the shape of the model to allow establishing correspondence of nodes in the images of the two cameras. This requirement becomes more important as the convergence angle between the cameras increases and corresponding points on the model appear more different as the camera perspective differences increase.

For the case of maximum model elongation, the automatic algorithm for establishing point correspondence failed because the model was so deformed in the initial images. Therefore, measurements were made only at ten points along a line near the model center, and points in image B corresponding to points in image A were located manually by eye and “point and click” with the computer mouse. The tediousness of this procedure precluded making measurements on more than this small number of points.

The plates with cut-outs that matched the elongation of the trellis included reference marks that appeared in the images of both cameras. The vertical positions of these marks were measured by photogrammetry and their average was taken as the reference zero position. Variations in the zero position among all configurations were less than 0.5 mm.

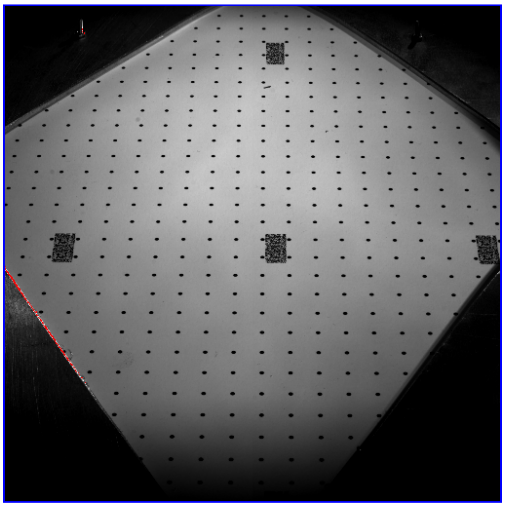

Figure 10. Image of calibration plate from one camera.

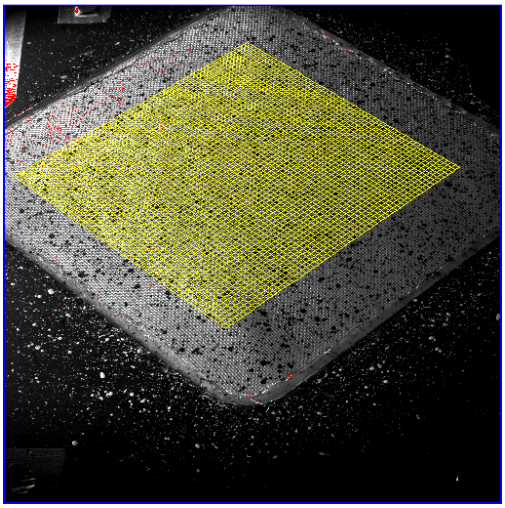

Figure 11. Interrogation grid projected into wind-off image of model with no elongation.

Test Matrix

Presented in table 2 is the test matrix that was followed during the first test entry. It should be noted that not all of the test points were actually achieved. In some cases, the fabric slipped or failed in the frame during the elongation process and in other cases, (with the F-111 fabric) the porosity of the fabric was so great that it was not possible to establish the desired differential pressure loading. Only the results of selected runs are presented in this report.

Table 2. Test matrix for phase 1.

Fabric	Panel Orient.	Tunnel Conditions	Frame Elongation (in.)	Measurements
Solid panel	N/A	M=0.46 No insert	N/A	Pitot probe b.l. surveys at 12, 24, 36, 48 inches
Solid panel	N/A	M=0.46 Insert	N/A	"
Uncoated Nylon (F-111)	Tension	M=0.46, ΔP_{fabric}=0 → 3.0, 0.5 psi No insert	0.0, 0.1, 0.2, 0.6, 1.2, 1.8	Tunnel conditions, Frame load cell load, Frame elongation, Fabric Δp, Fabric Deformation, PIV
"	Shear	"	0.0, 0.6, 1.2, 1.8, 2.4	"
Silicon coated Kevlar (ST11-4600)	Tension	"	0.0, 0.1, 0.2, 0.6	"
"	Shear	"	0.0, 0.6, 1.2, 1.8, 2.4	"
Uncoated Nylon (F-111)	Tension	M=0..46, ΔP_{fabric}=0 → 3.0, 0.5 psi Wall insert	0.0, 0.1, 0.2, 0.6, 1.2, 1.8	Tunnel conditions, Frame load cell load, Frame elongation, Fabric Δp, Fabric Deformation, PIV
"	Shear	"	0.0, 0.6, 1.2, 1.8, 2.4	"
Silicon coated Kevlar (ST11-4600)	Tension	"	0.0, 0.1, 0.2, 0.6	"
"	Shear	"	0.0, 0.6, 1.2, 1.8, 2.4	"

RESULTS

Presented in this section is the data acquired from two test entries (referred to as Phase 1 and Phase 2). Minor refinements were made to the measurement systems as will be described to improve the data quality between the first and second entry.

Phase 1 Tests

Figure 12 shows the relative positions of the PIV and photogrammetry measurement regions and the coordinates used to report the data. X is streamwise (0 at the laser sheet, positive downstream), Y is cross-stream (0 at the tunnel centerline, positive away from the laser), and Z is vertical (0 at the test section floor, positive up). The figure includes a red line in the photogrammetry plane that shows where the contour data were cross cut to yield displacement profiles.

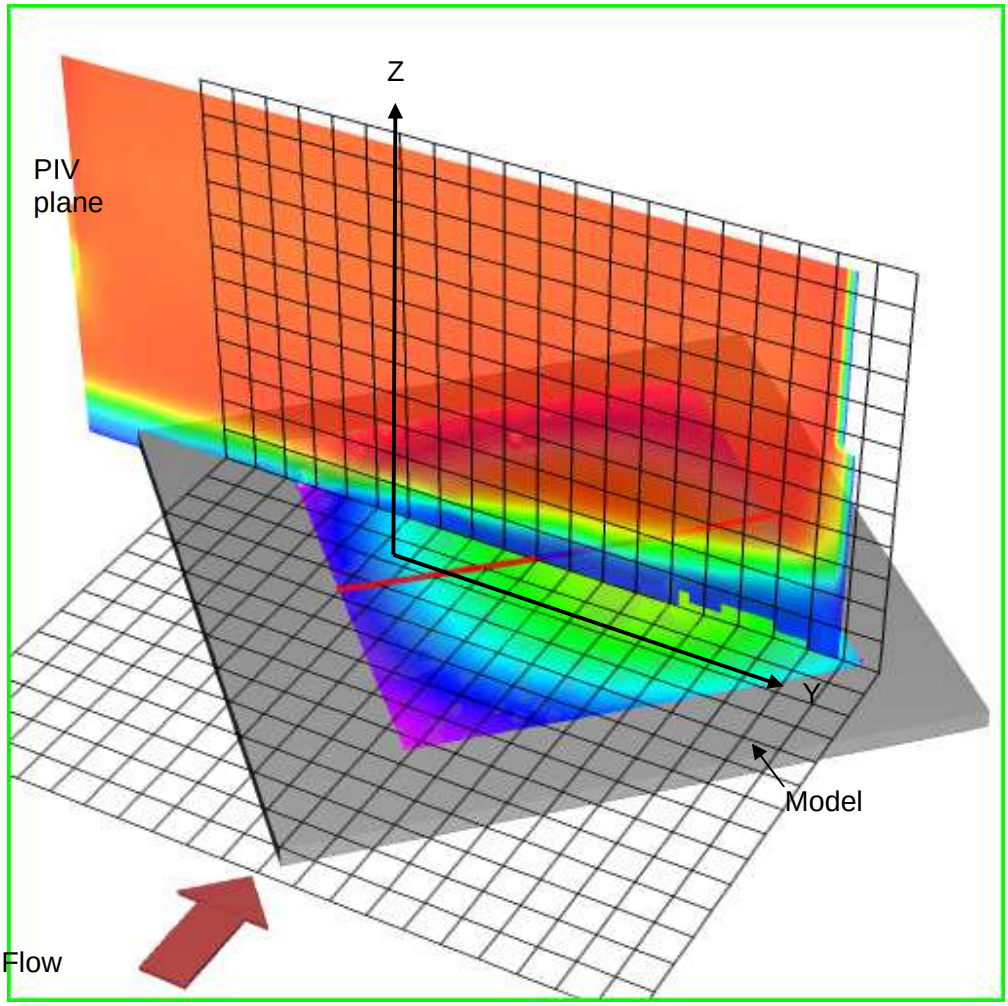

Figure 12. PIV and photogrammetry measurement planes and coordinate systems. Grid cells are 1 x 1 cm.

Velocity Measurements

Presented in figures 13 through 36 are the results of the PIV measurements. Shown are contours of the X-component of velocity with cross flow velocity vectors superimposed. Figures 13-22 are for cases without the circular arc wall insert present, and Figures 23-36 show data obtained with the wall insert present. Listed in the figure captions is the desired pressure differential between the plenum below the fabric and the tunnel free stream static pressure measured at the entrance to the test section. The pressure, load data and other measured parameters can be found in the table in appendix A. The fabric weave orientation was in the shear orientation (i.e. fabric yarn direction initially aligned with the side edges of the frame) for the cases shown.

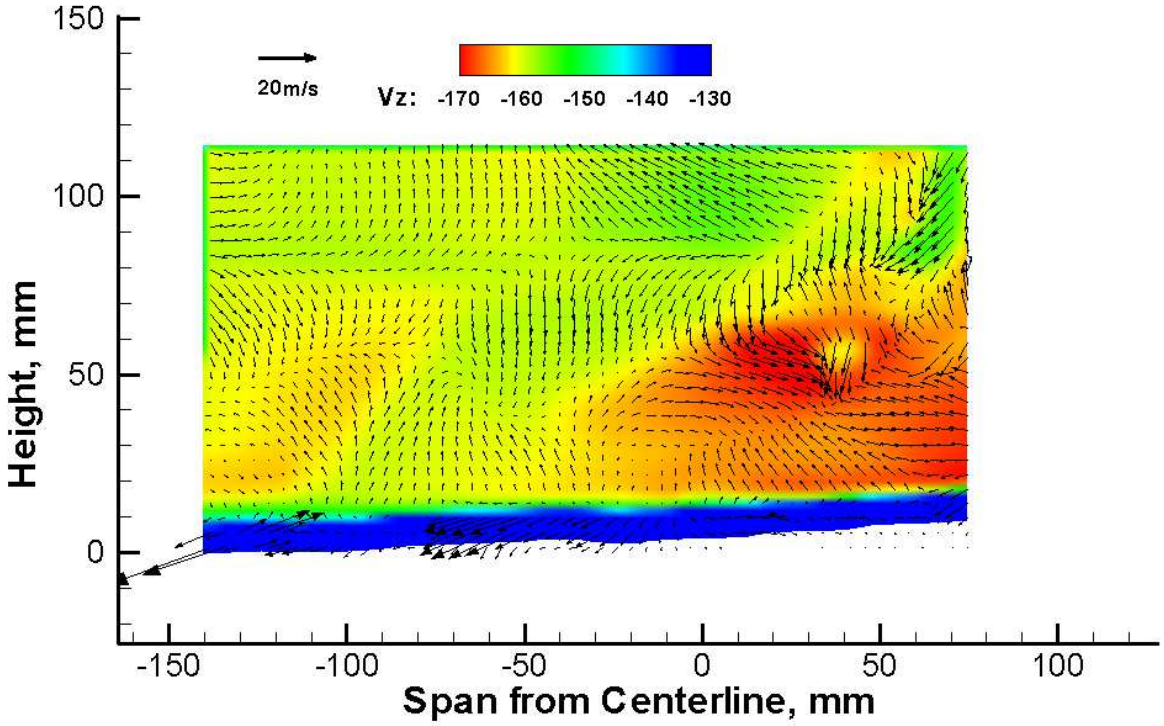

Figure 13. Stream-wise velocity at the initial elongation of 0 inch and ΔP =0.011 psi.

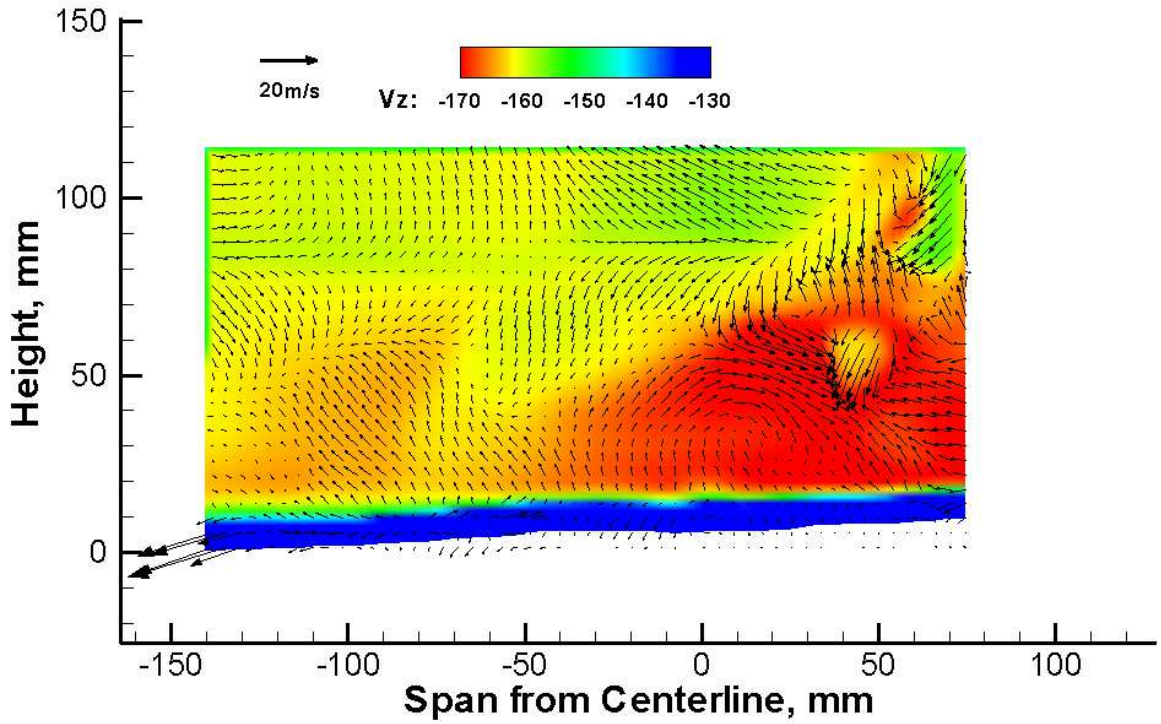

Figure 14. Stream-wise velocity at the initial elongation of 0 inch and ΔP=1.462 psi.

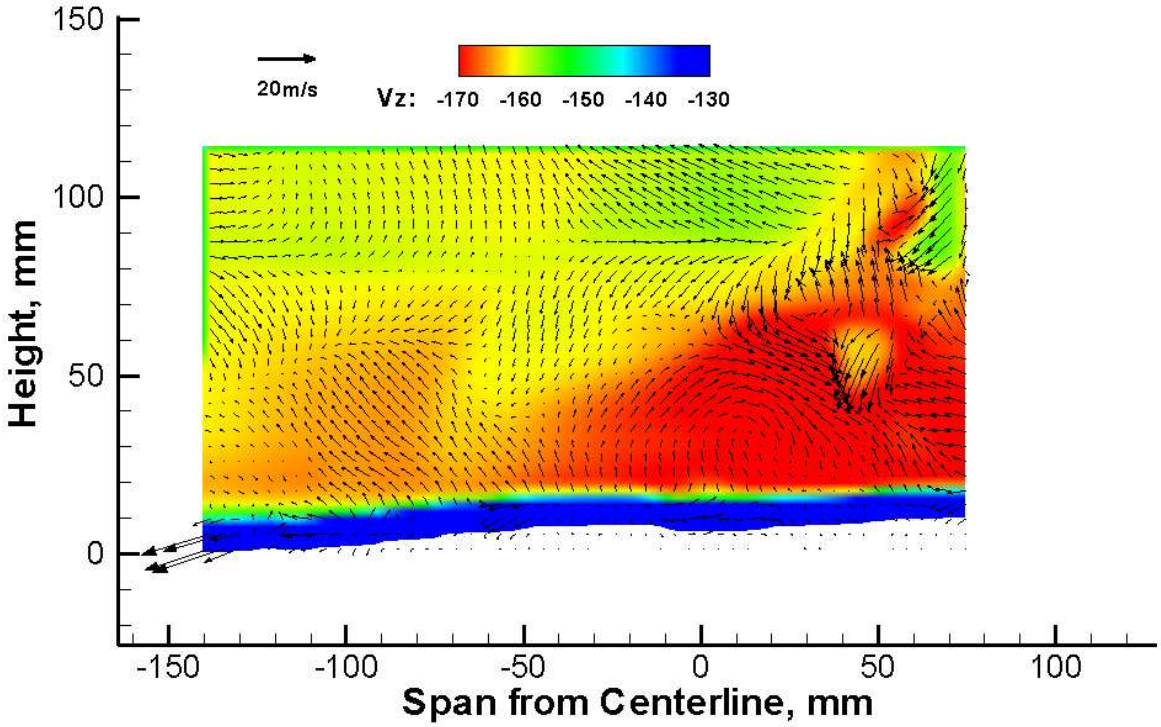

Figure 15. Stream-wise velocity at the initial elongation of 0 inch and ΔP=2.416 psi.

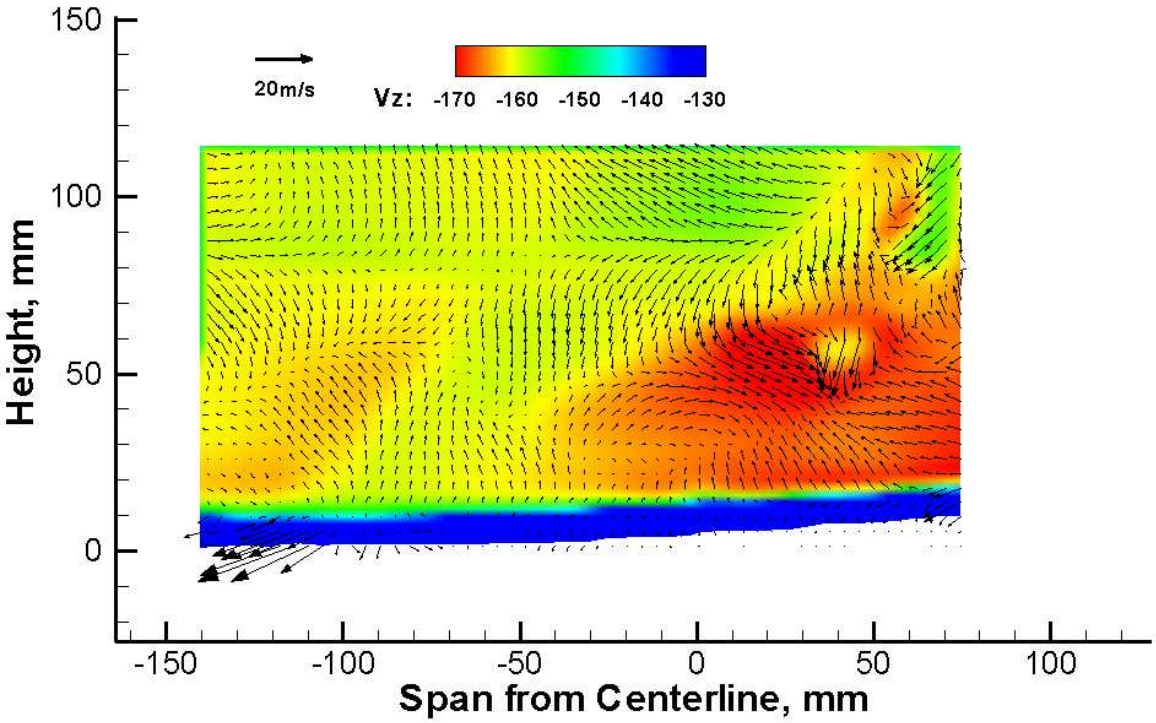

Figure 16. Stream-wise velocity at 0.6 inch elongation and ΔP=0.028 psi.

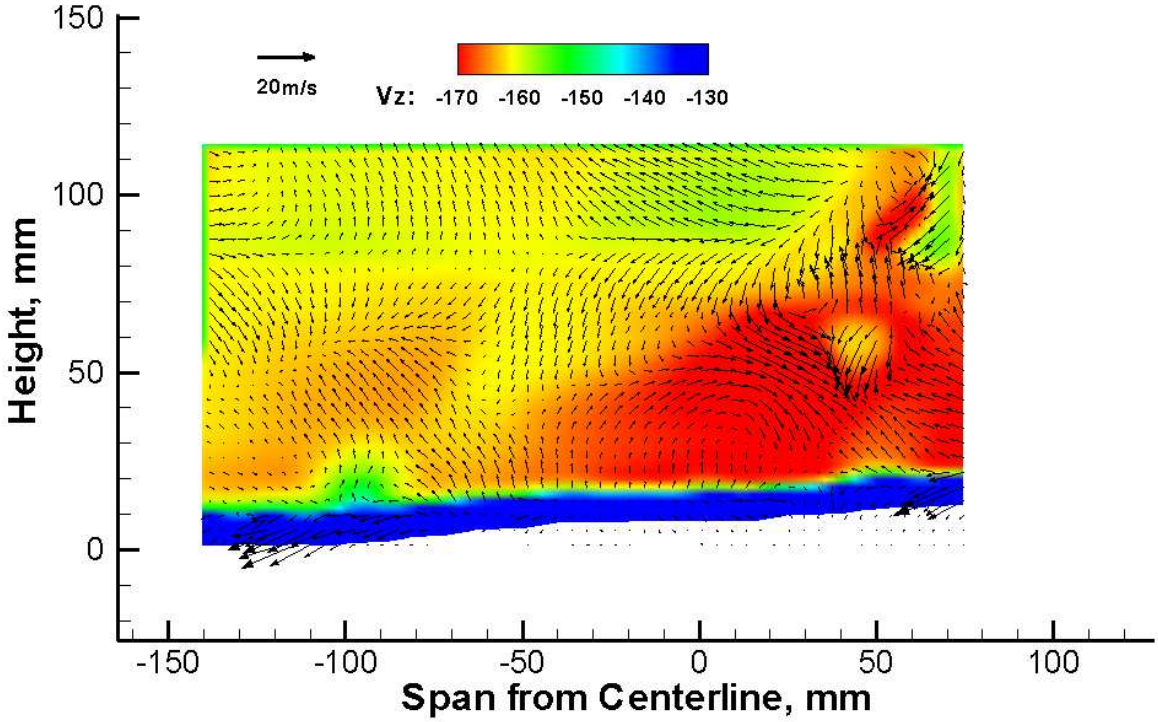

Figure 17. Stream-wise velocity at 0.6 inch elongation and ΔP=0.992 psi.

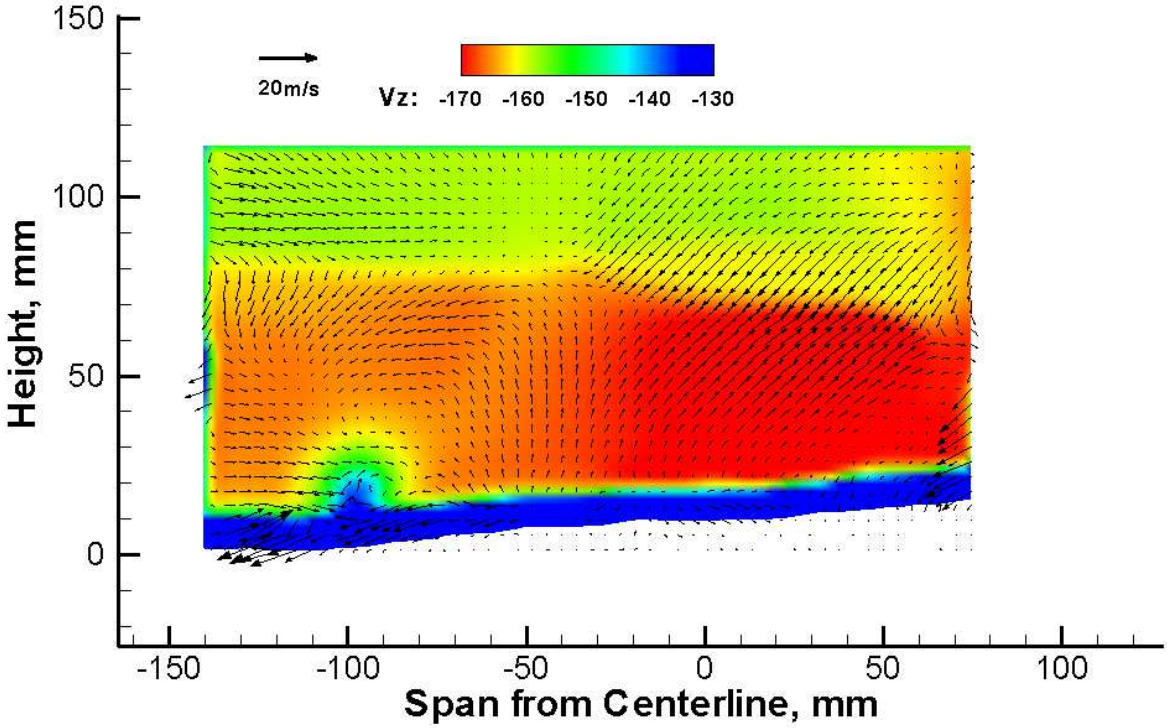

Figure 18. Stream-wise velocity at 0.6 inch elongation and ΔP=1.447 psi.

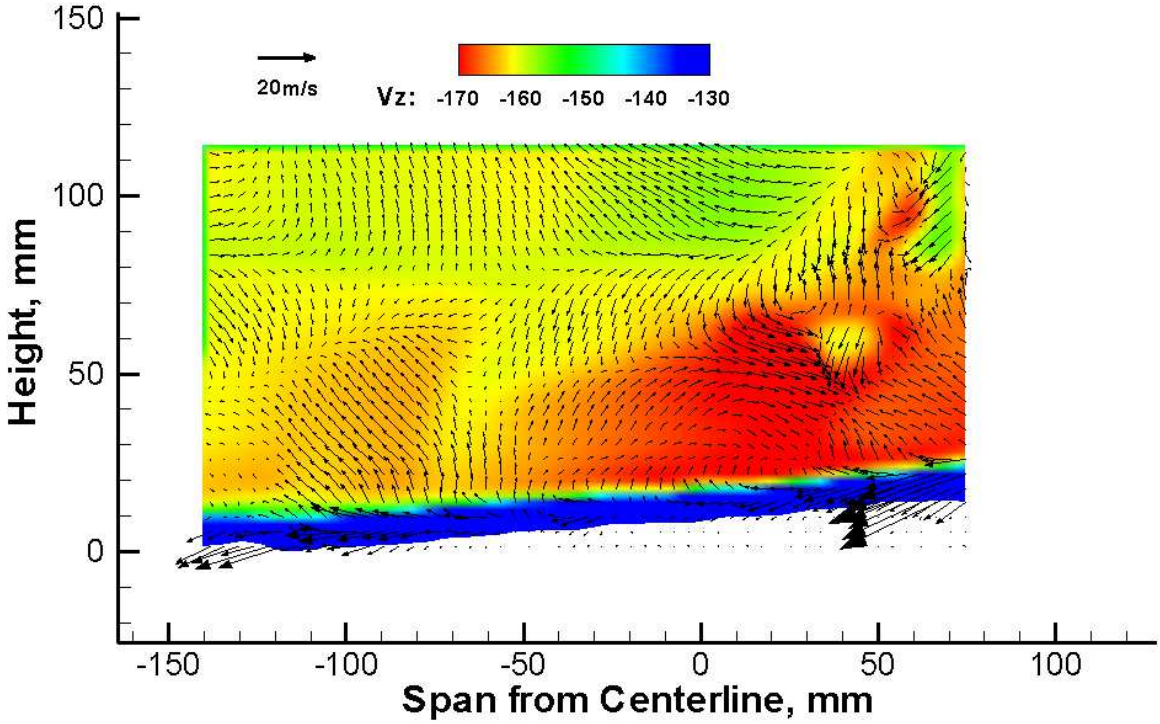

Figure 19. Stream-wise velocity at 1.2 inch elongation and ΔP=0.013 psi.

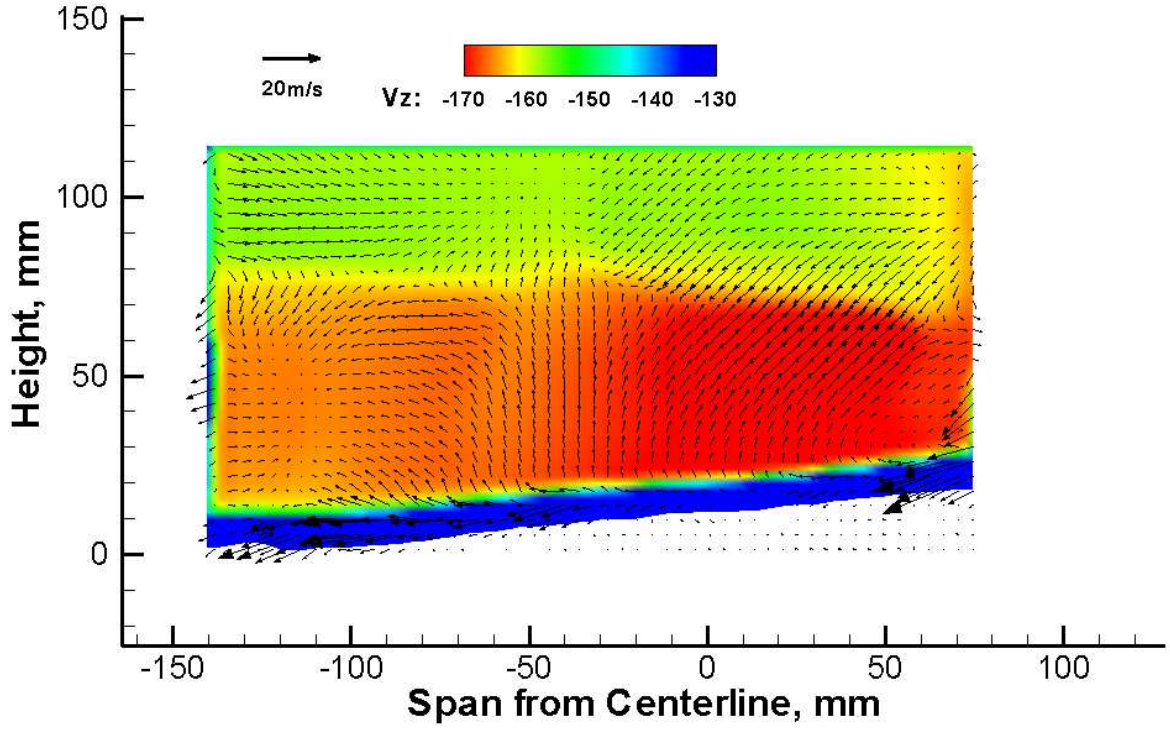

Figure 20. Stream-wise velocity at 1.2 inch elongation and ΔP=0.960 psi.

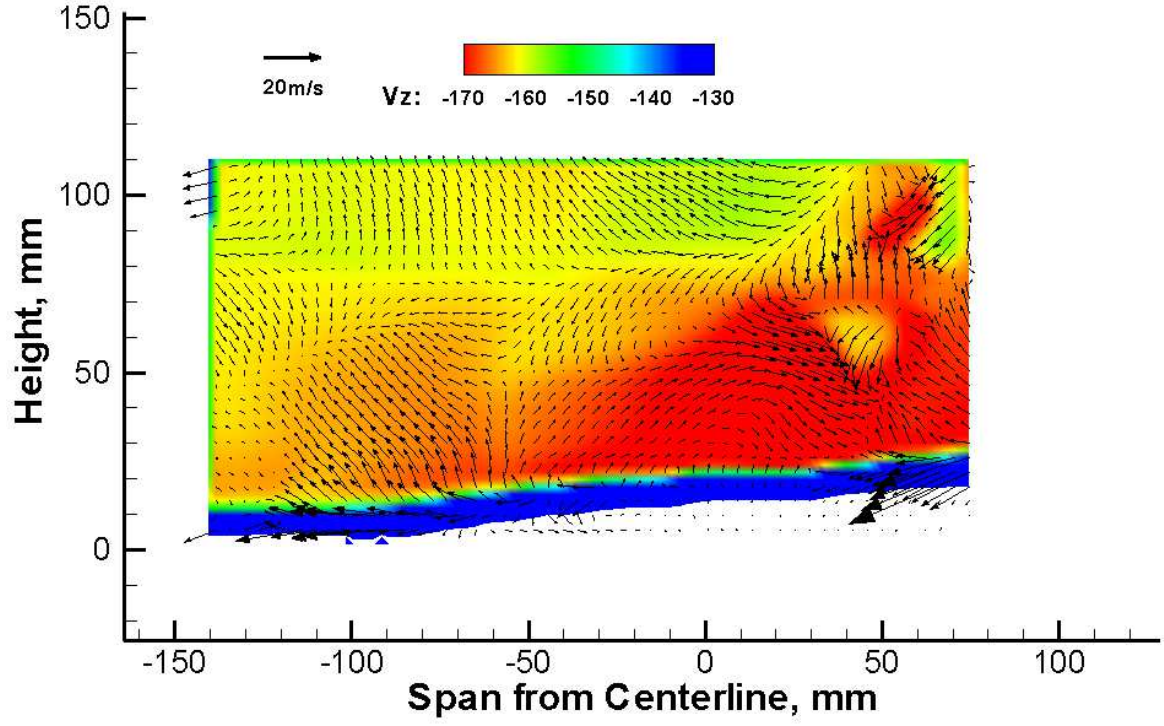

Figure 21. Stream-wise velocity at 1.2 inch elongation and ΔP=1.970.

Figure 22. Not available.

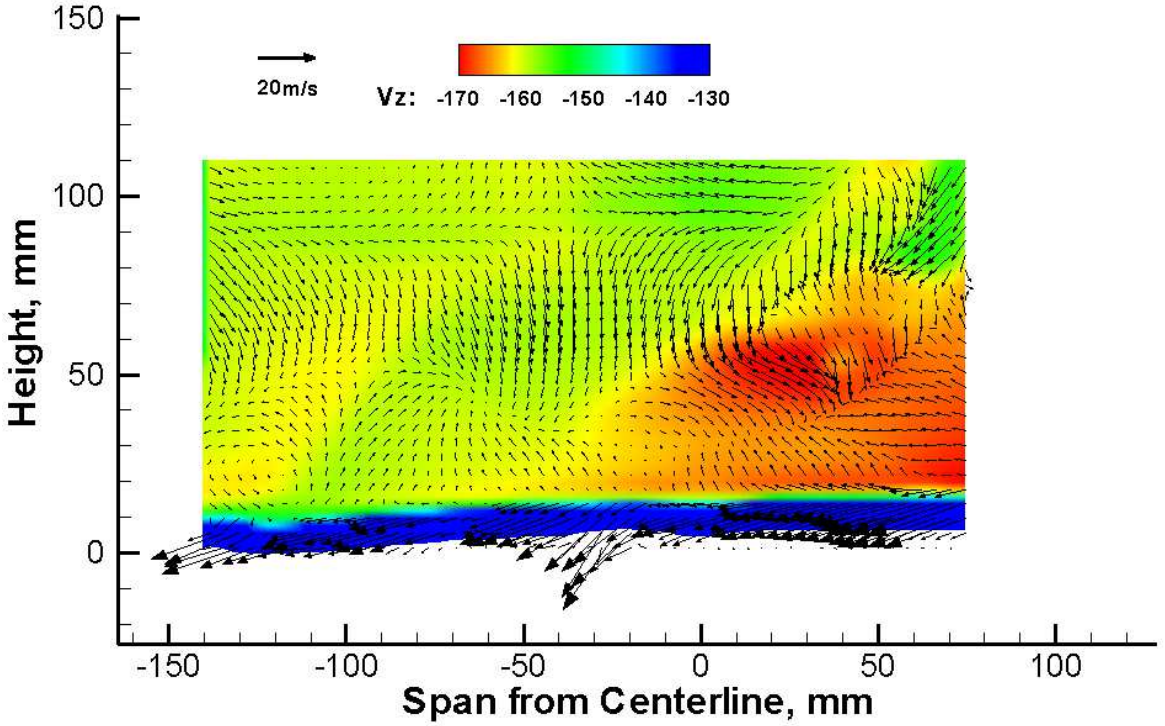

Figure 23. Stream-wise velocity at the initial elongation of 0 inch and ΔP=0.015 psi.

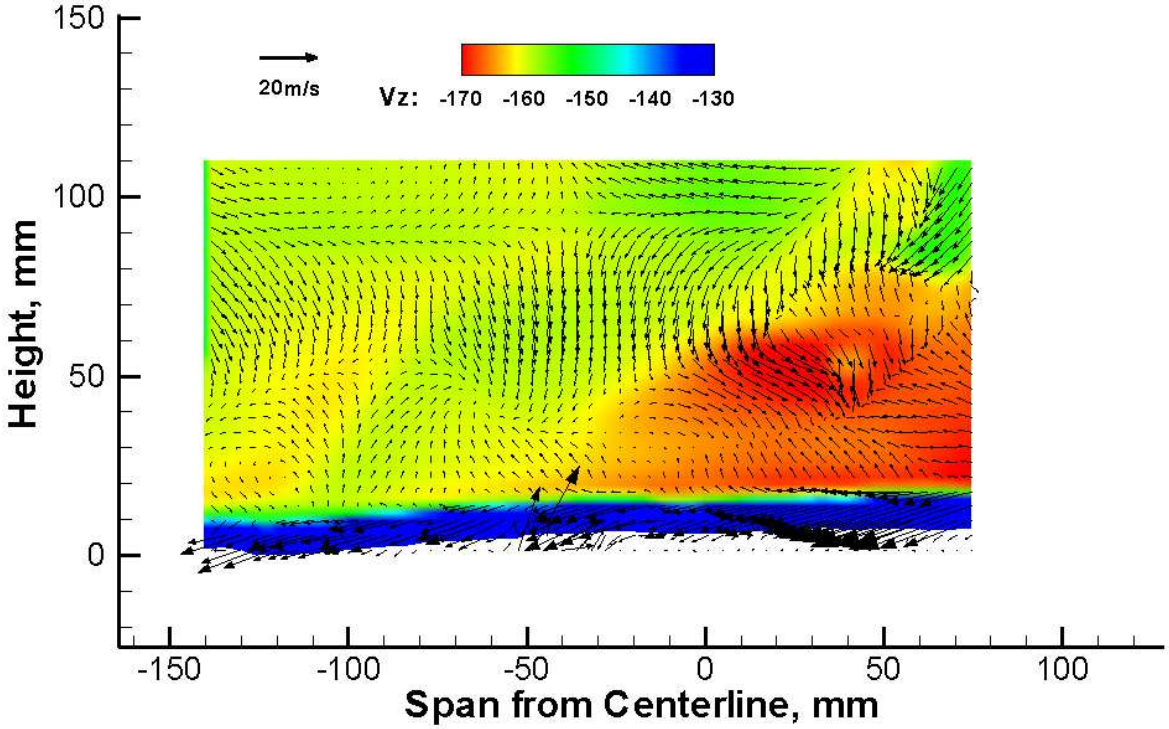

Figure 24. Stream-wise velocity at the initial elongation of 0 inch and ΔP=0.513 psi.

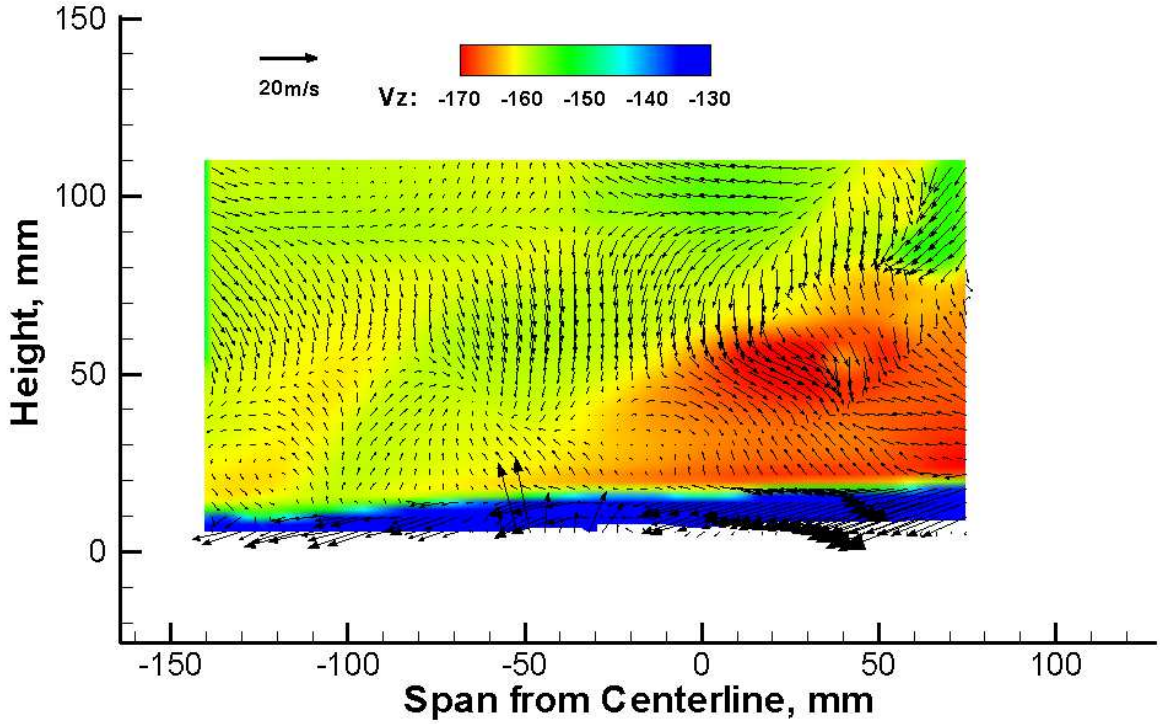

Figure 25. Stream-wise velocity at the initial elongation of 0 inch and ΔP=0.497 psi.

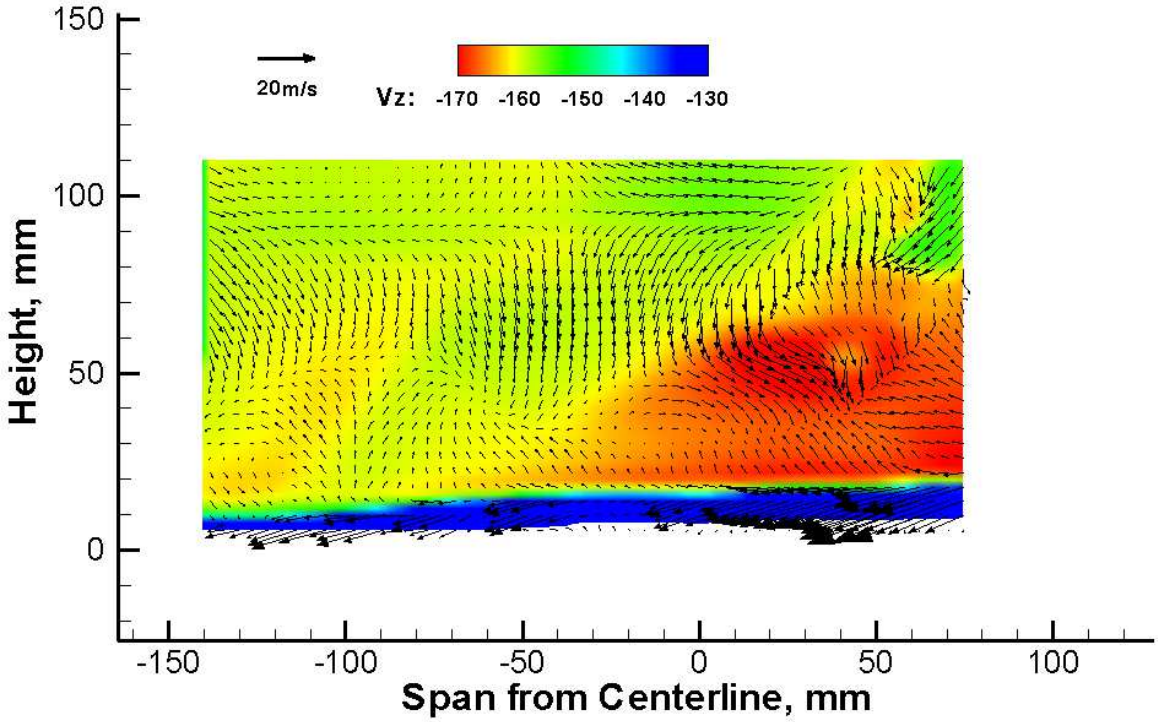

Figure 26. Stream-wise velocity at the initial elongation of 0 inch and ΔP=1.028 psi.

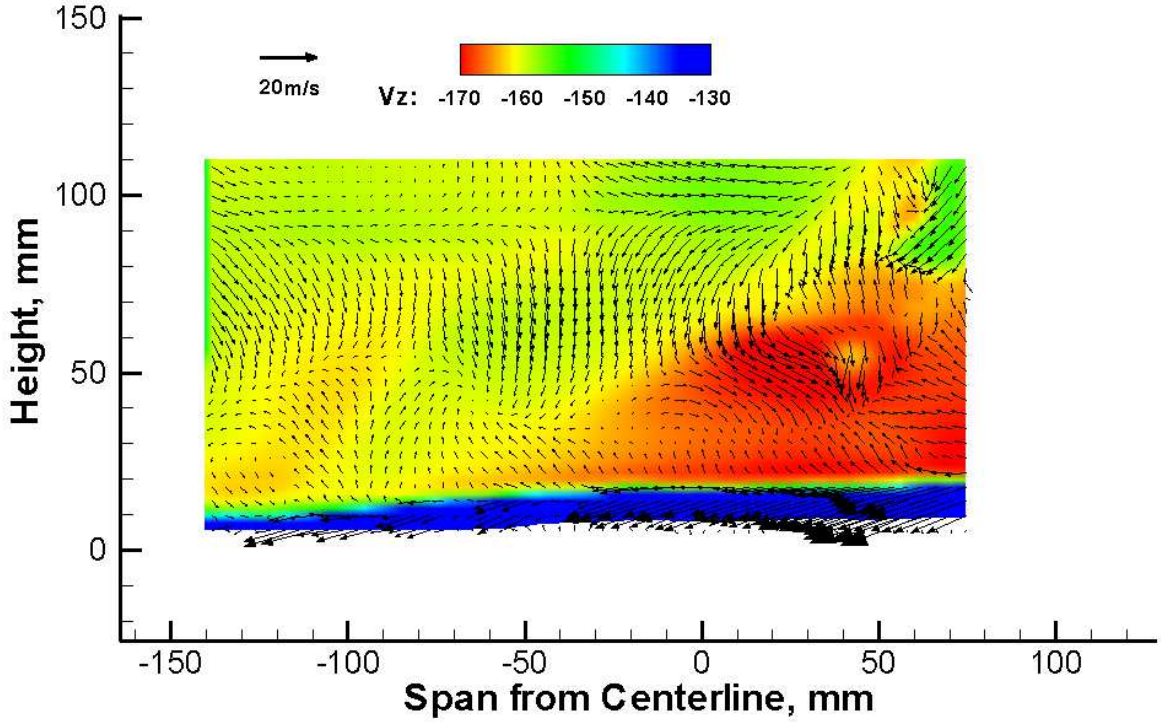

Figure 27. Stream-wise velocity at the initial elongation of 0 inch and ΔP=1.028 psi (repeat).

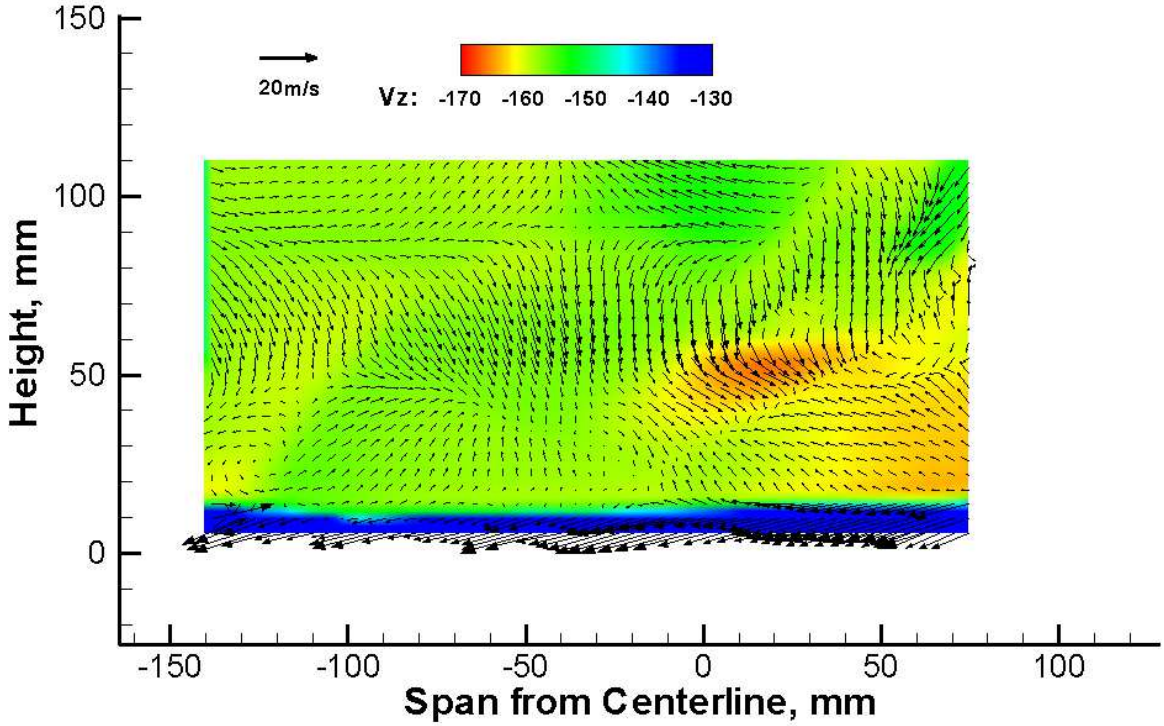

Figure 28. Stream-wise velocity at 0.6 inch elongation and ΔP=0.015 psi.

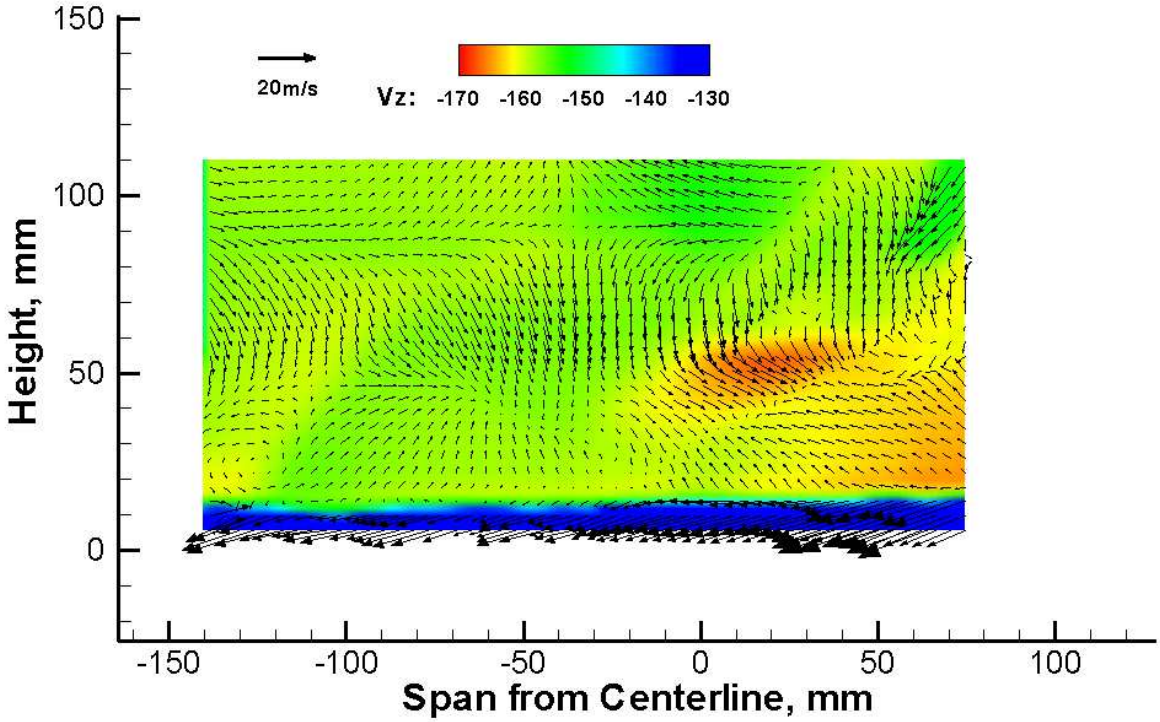

Figure 29. Stream-wise velocity at 0.6 inch elongation and ΔP=0.512 psi.

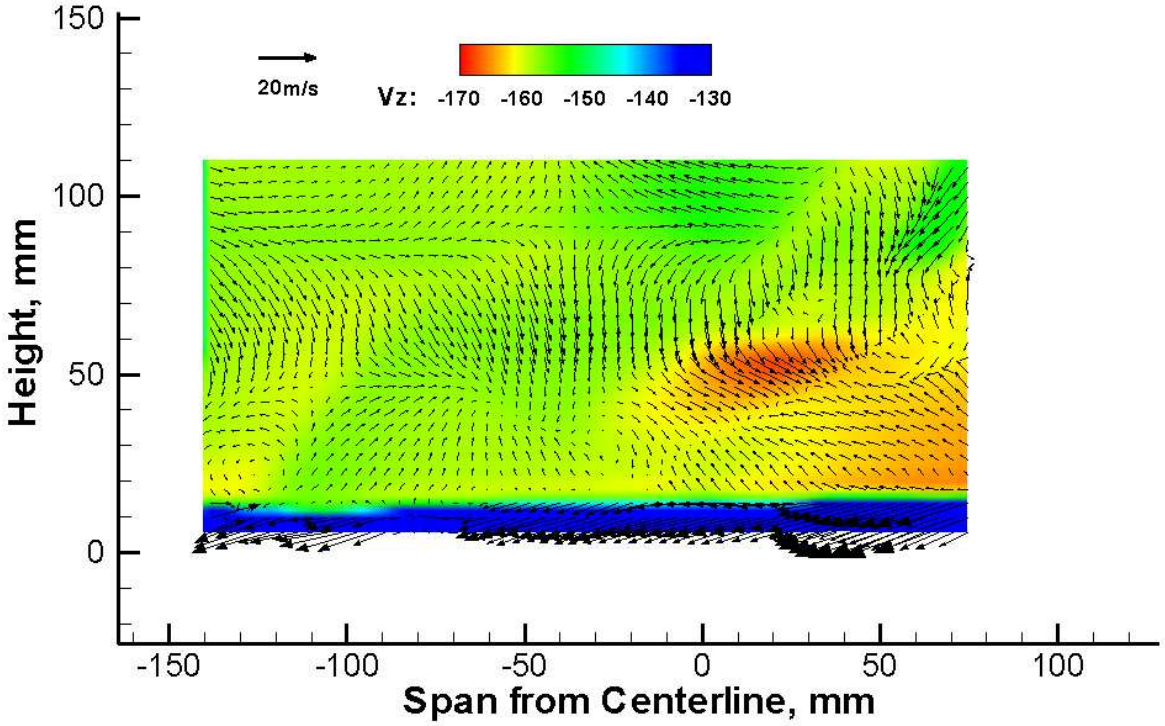

Figure 30. Stream-wise velocity at 0.6 inch elongation and ΔP=1.017 psi.

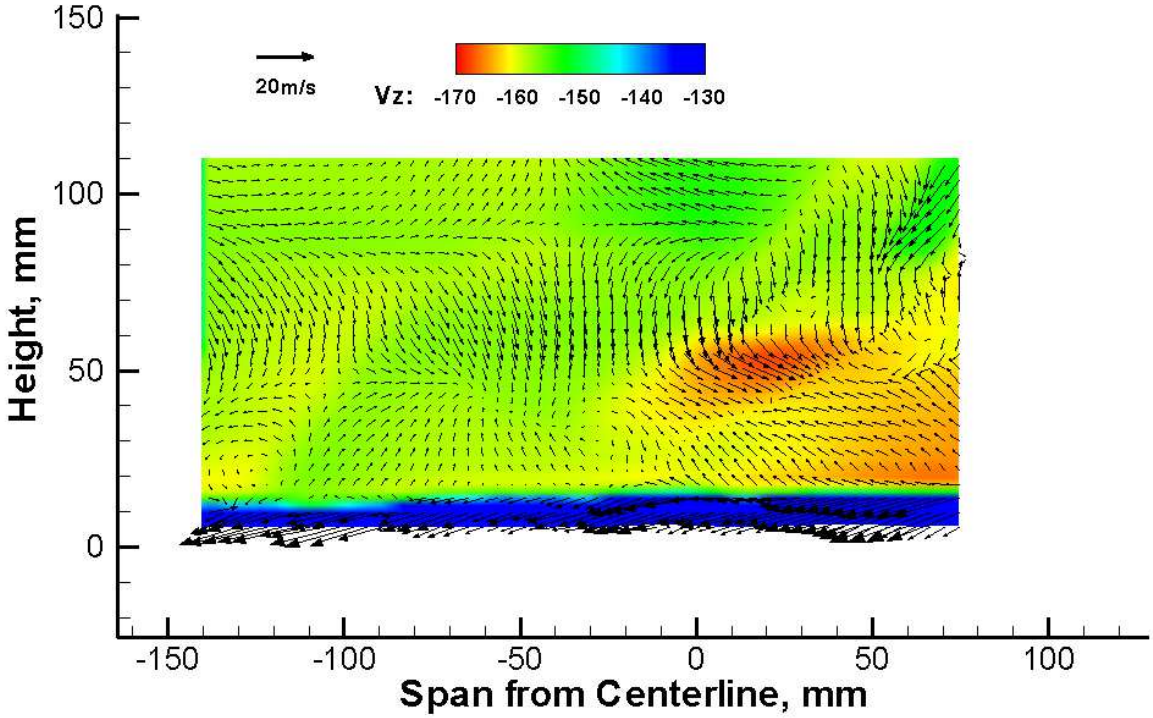

Figure 31. Stream-wise velocity at 0.6 inch elongation and ΔP=1.507 psi.

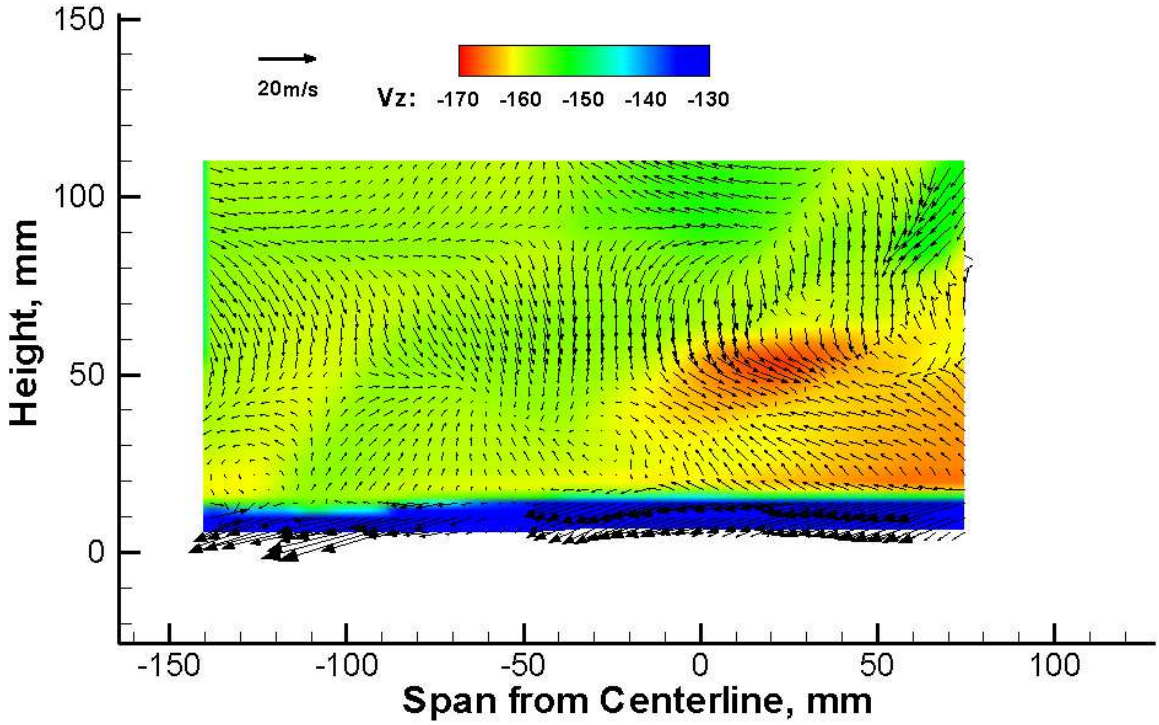

Figure 32. Stream-wise velocity at 0.6 inch elongation and ΔP=1.507 psi (repeat).

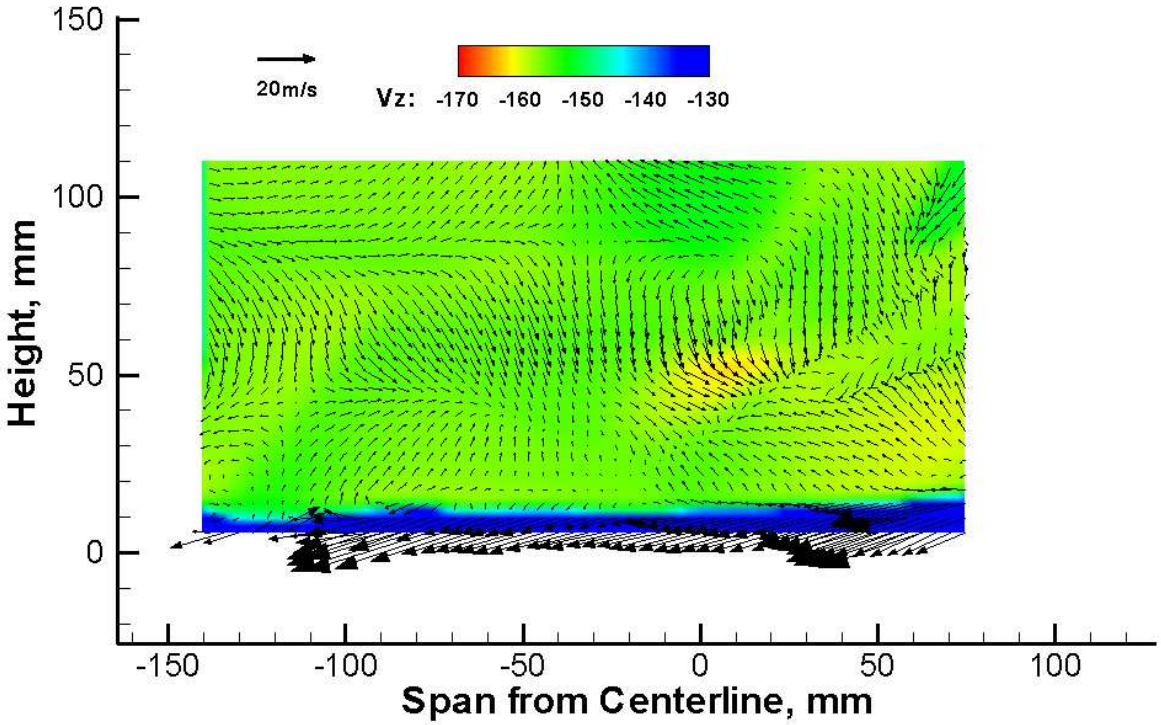

Figure 33. Stream-wise velocity at 1.2 inch elongation and ΔP=0.029 psi.

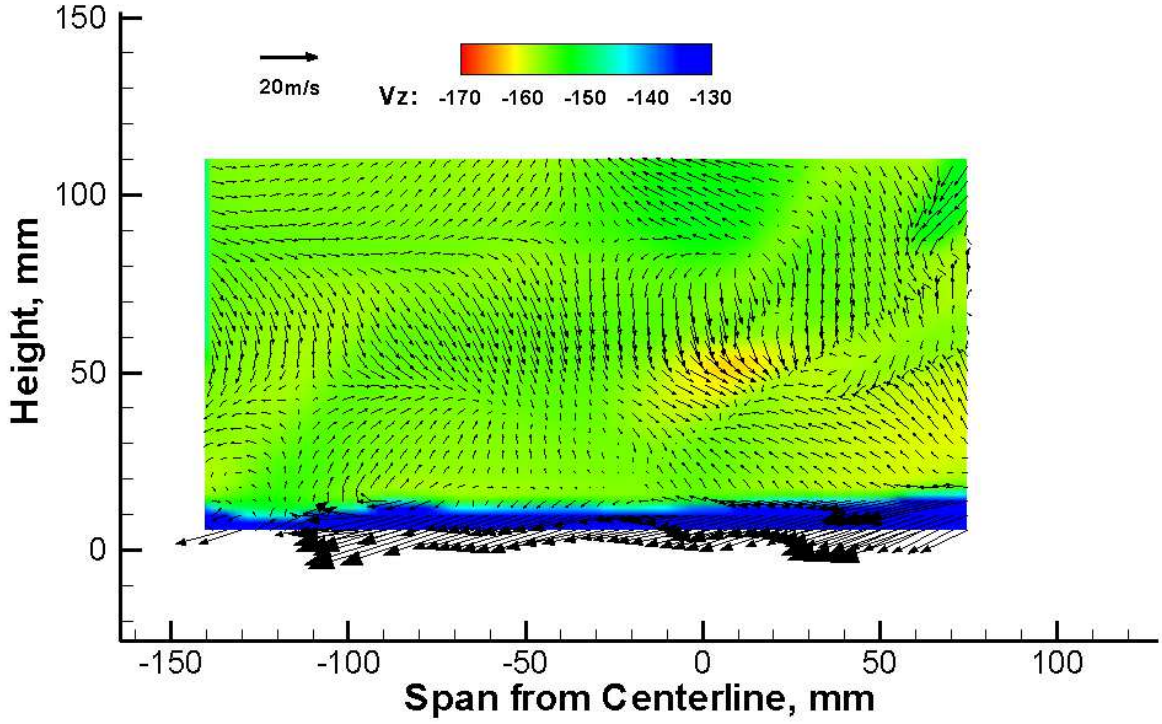

Figure 34. Stream-wise velocity at 1.2 inch elongation and ΔP=0.516 psi.

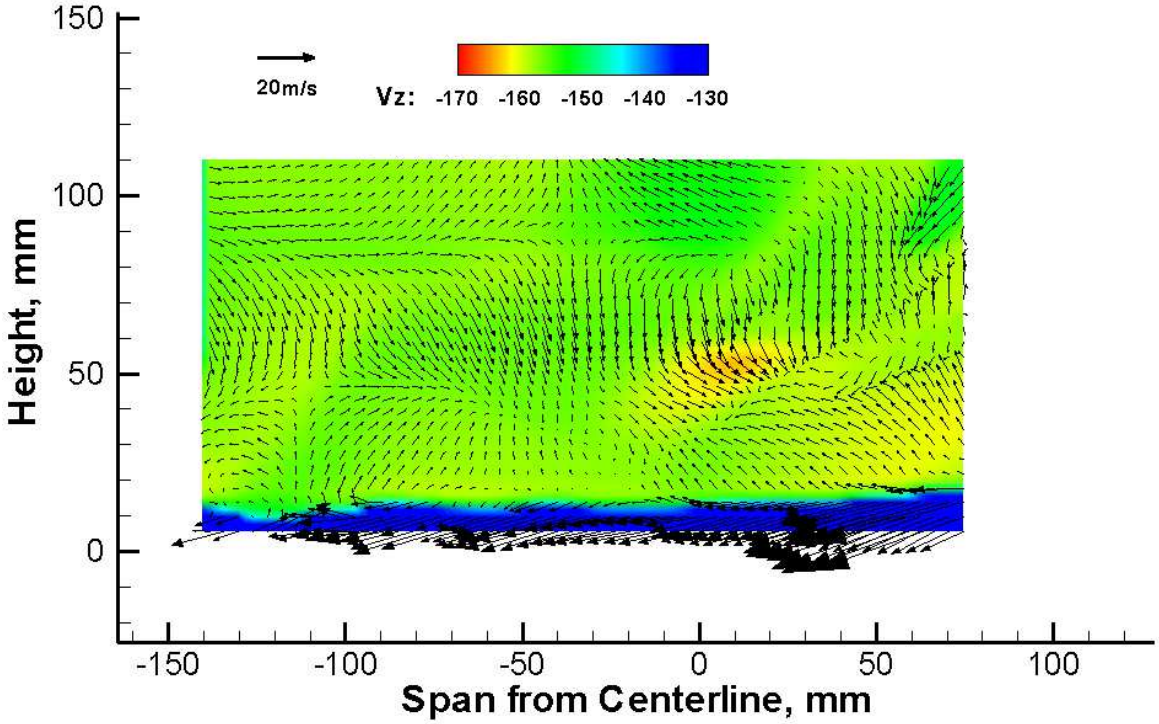

Figure 35. Stream-wise velocity at 1.2 inch elongation and ΔP=0.998 psi.

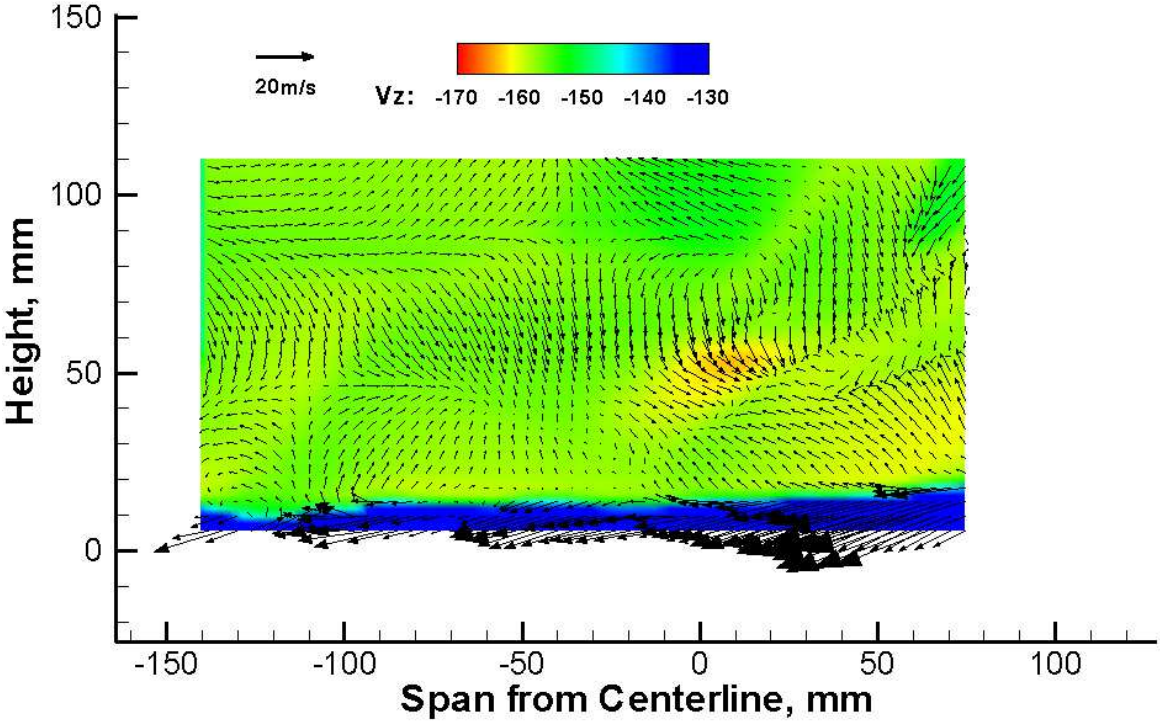

Figure 36. Stream-wise velocity at 1.2 inch elongation and ΔP=1.509 psi.

Deformation Measurements

Model displacements were measured at each node of a rectangular 60x60-node interrogation grid that was rotated 45° with respect to the tunnel axes to match the orientation of the model (Fig. 11). Model features at each node were tracked through the sequence of images as the plenum pressure was changed. Figure 37 shows the time history of the out-of-plane (z) displacement of a point near the center of a Kevlar model for the case of no elongation and a flat ceiling. It includes tunnel start-up with zero pressure difference between the plenum and the test section; five intervals where the plenum pressure was increased in 0.5 psi increments; and tunnel shutdown. Note that at each plenum pressure the displacement of the model was still slowly increasing when the next pressure was applied. This time history was typical of all runs.

Model displacements at each elongation and plenum pressure are shown as color-contour overlays of images of the model from the downstream camera (Figs. 38-40 and 42-44). The measurements correspond to data at the end of each pressure interval. The upstream corner of the model is at the top of each image. Figures 38, 39, and 40 show data for model elongations of 0, 0.6, and 1.2, respectively, for a flat top wall. No contour data are shown for the largest model elongation (1.8) because the automatic algorithm for establishing point correspondence failed in this case. Thus, ten correspondence points were located manually, "by eye," and are shown in Figure 41. Figures 42, 43, and 44 show data over elongations 0, 0.6, and 1.2, respectively, with the circular-arc top wall. Data at the larger elongations include many outliers that are clearly bad data points.

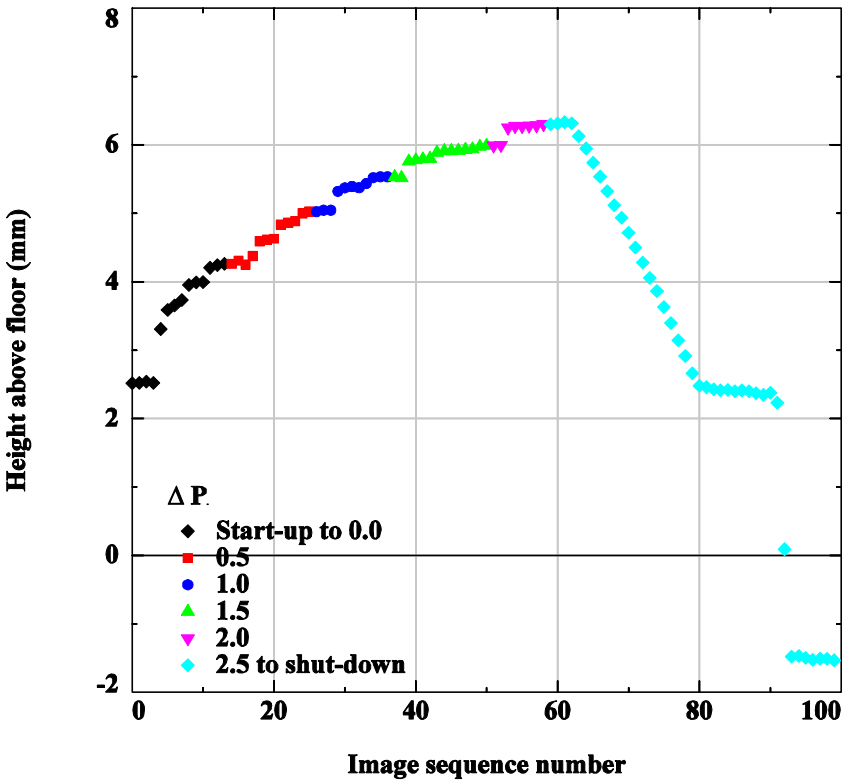

Figure 37. Time history of displacement near center of model (Run 21, Kevlar model, elongation = 0, flat ceiling).

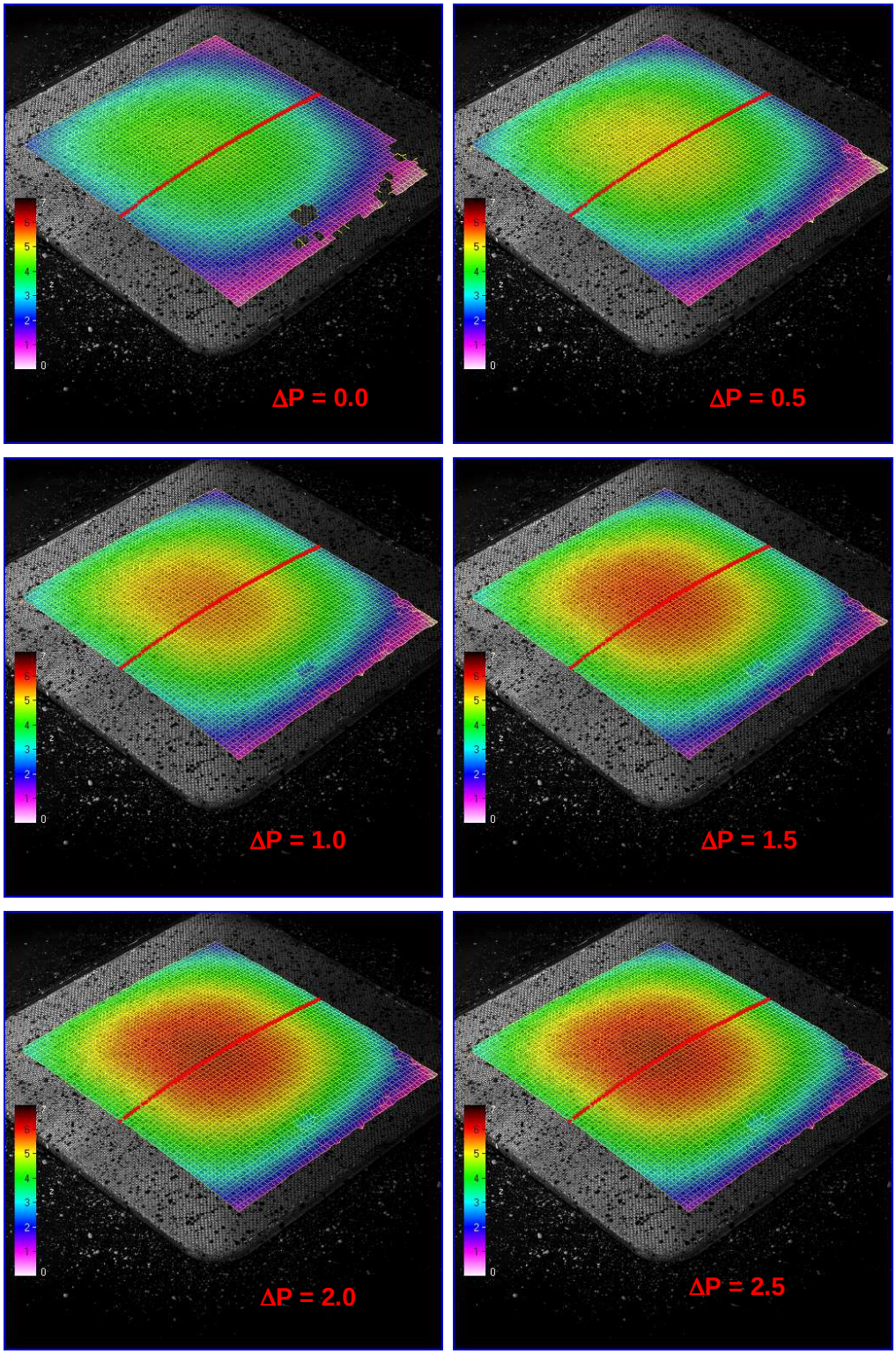

Figure 38. Effect of plenum pressure on out-of-plane displacements (Run 21, Kevlar model, elongation = 0, flat ceiling).

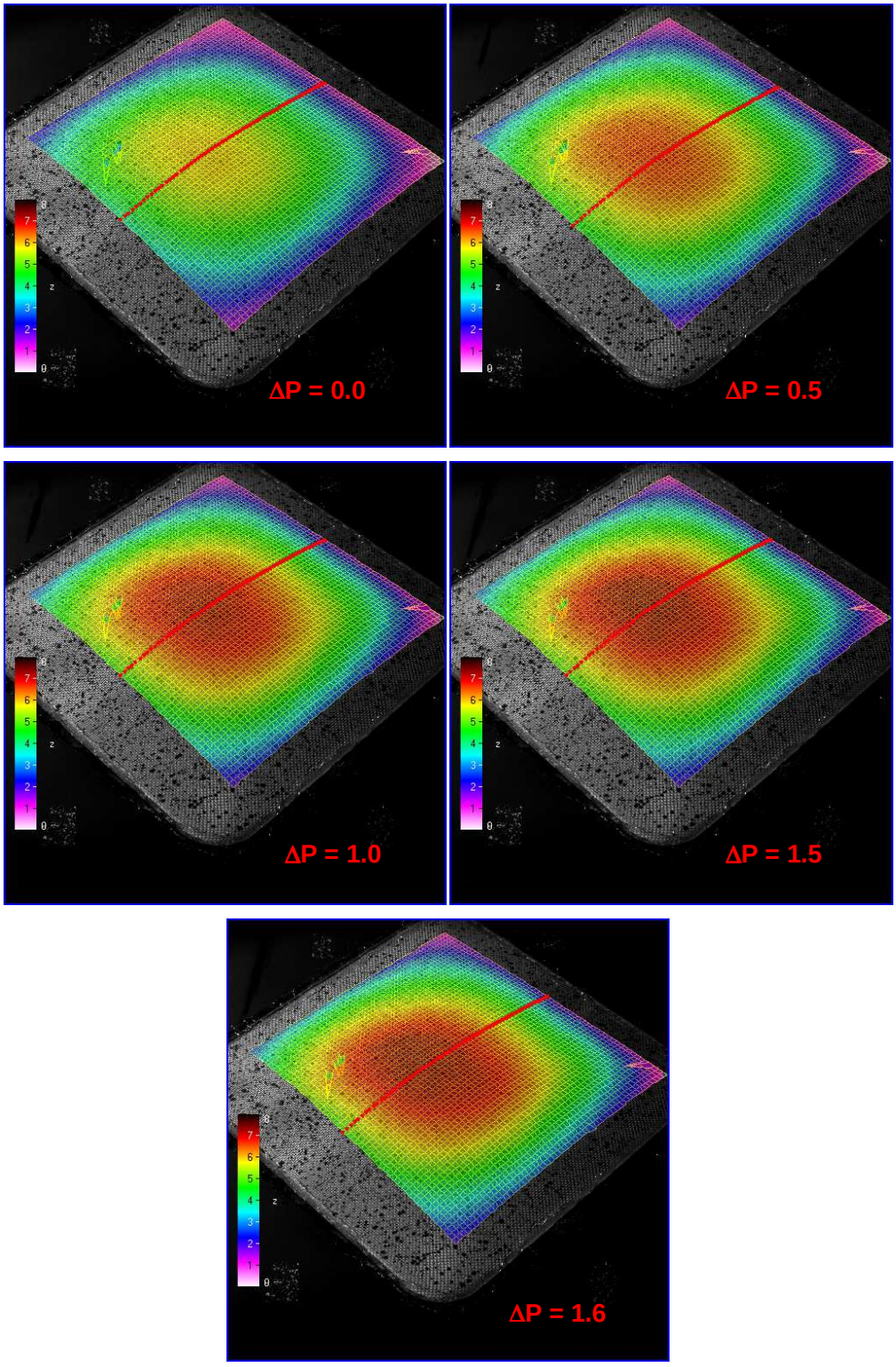

Figure 39. Effect of plenum pressure on out-of-plane displacements (Run 22, Kevlar model, elongation = 0.6, flat ceiling).

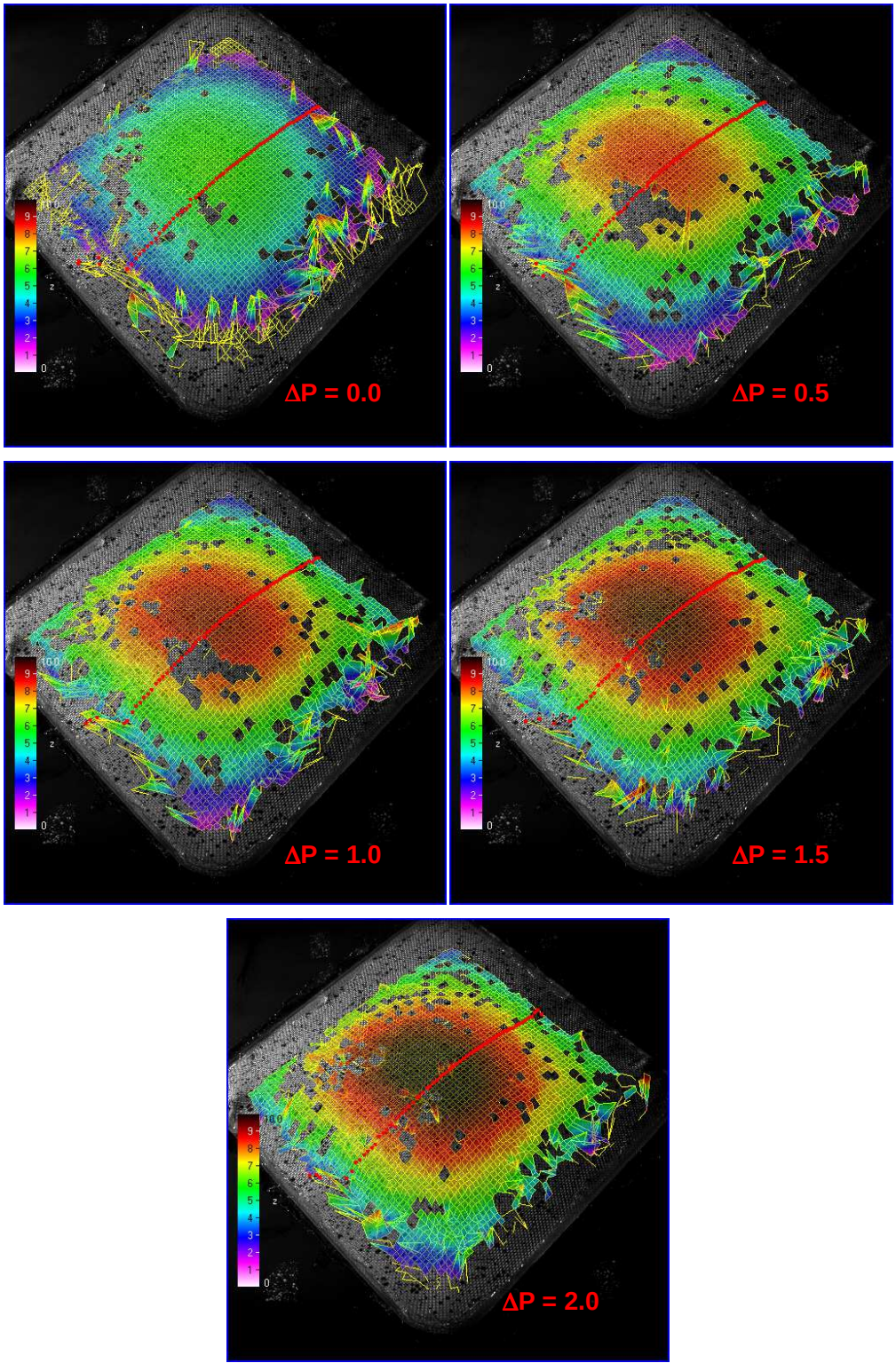

Figure 40. Effect of plenum pressure on out-of-plane displacements (Run 23, Kevlar model, elongation = 1.2, flat ceiling).

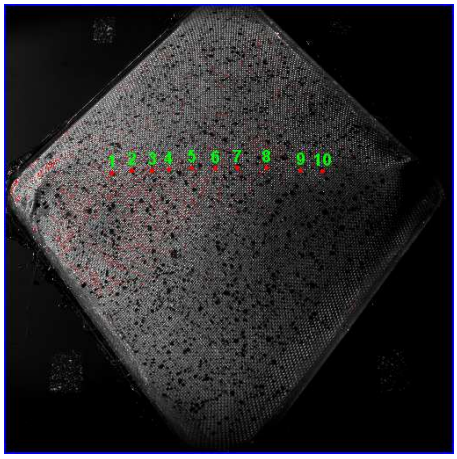

Figure 41. Manually located points for out-of-plane displacements measurements (Run 24, Kevlar model, elongation = 1.8, flat ceiling).

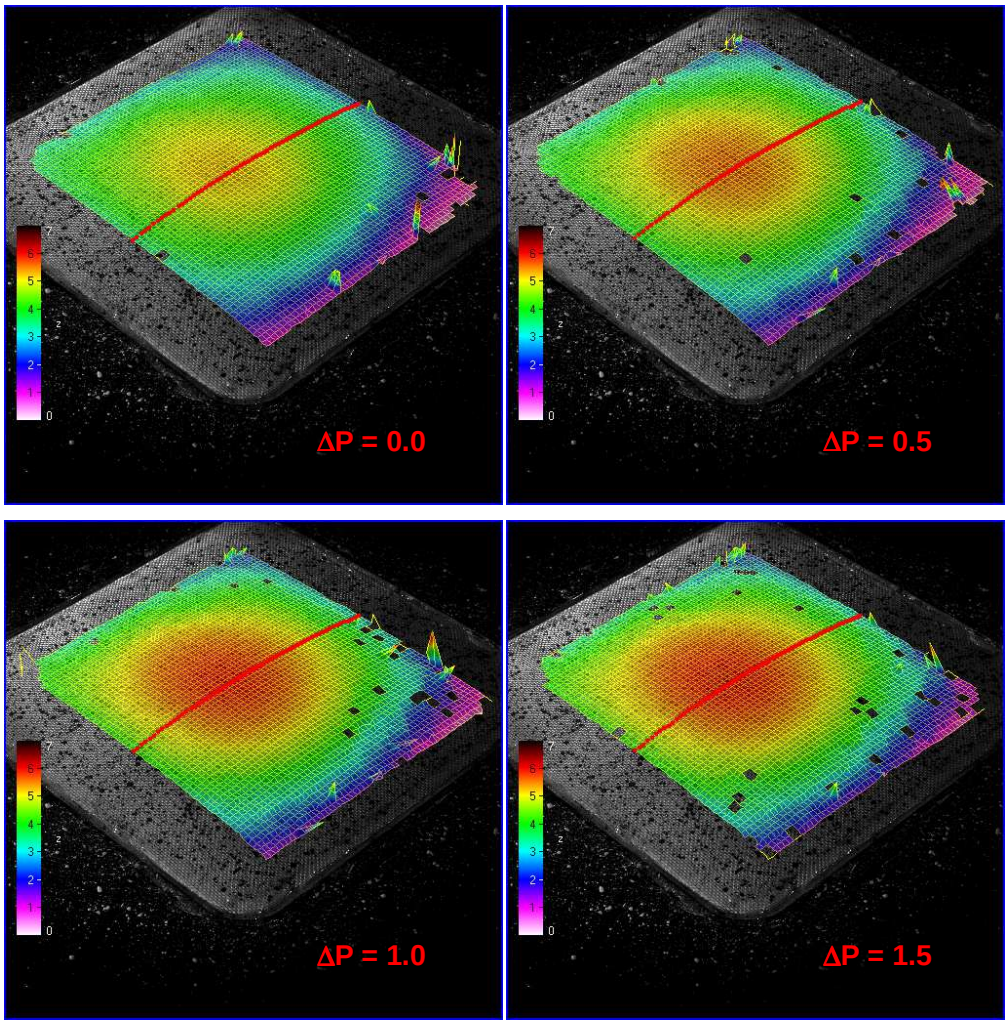

Figure 42. Effect of plenum pressure on out-of-plane displacements (Run 37, Kevlar model, elongation = 0, circular arc ceiling).

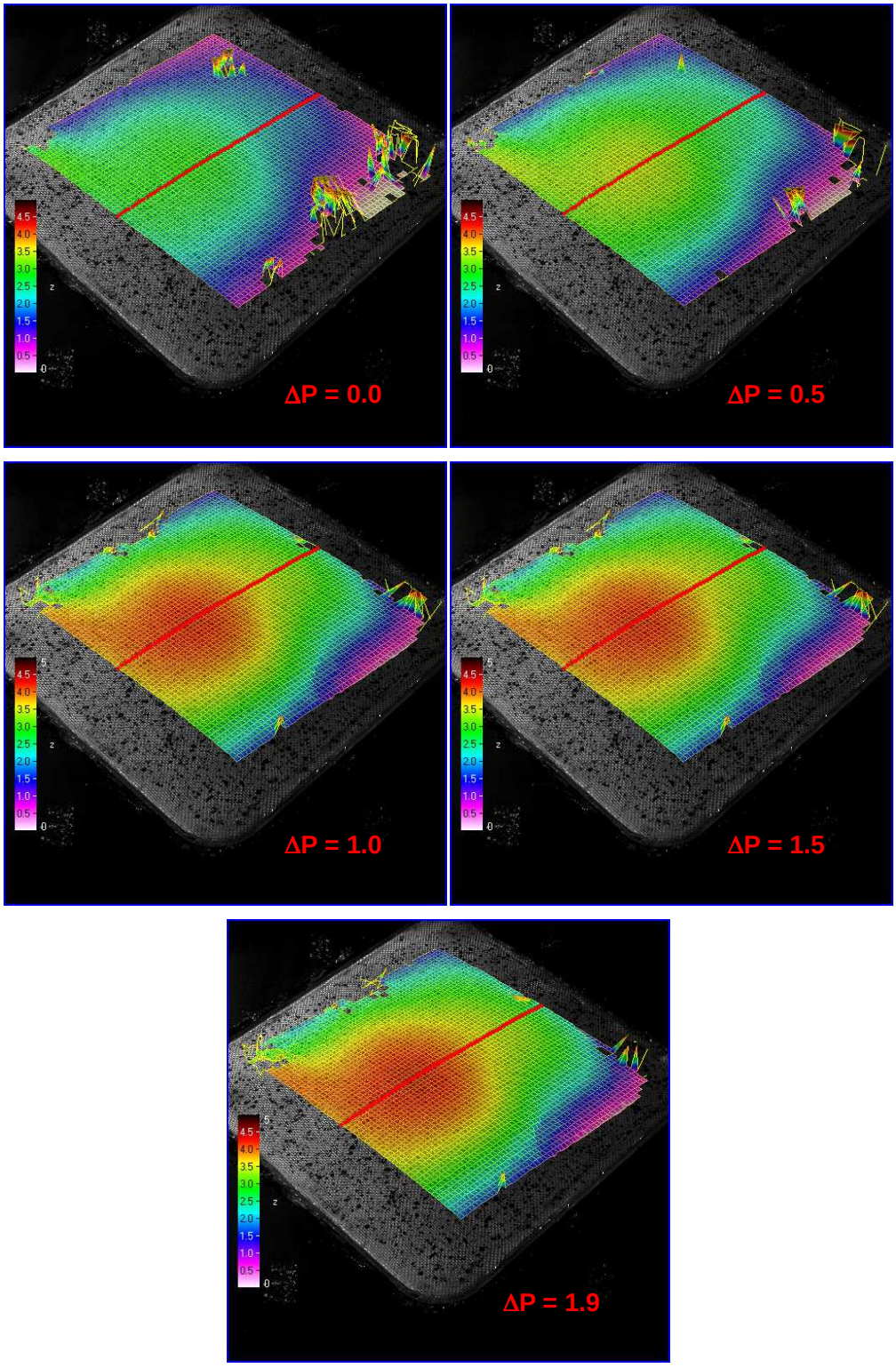

Figure 43. Effect of plenum pressure on out-of-plane displacements (Run 38, Kevlar model, elongation = 0.6, circular arc ceiling).

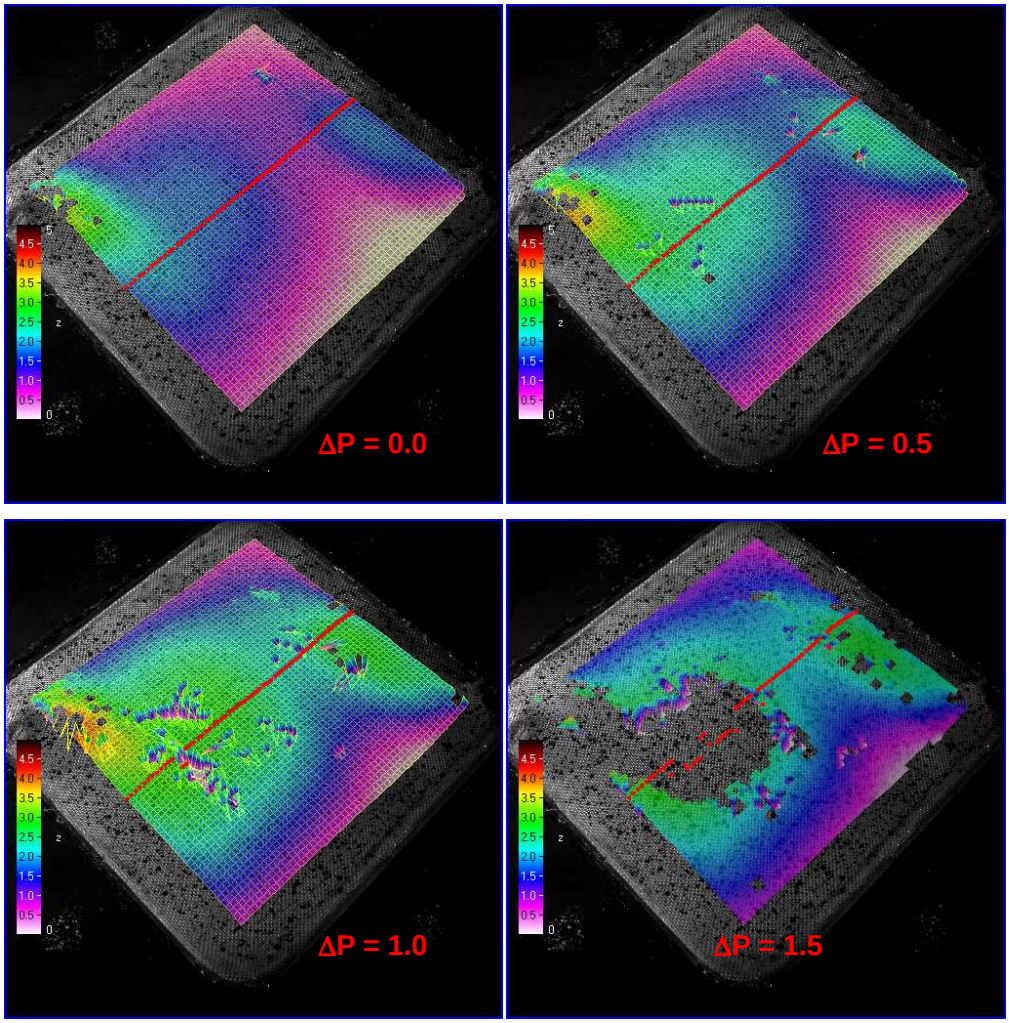

Figure 44. Effect of plenum pressure on out-of-plane displacements (Run 39, Kevlar model, elongation = 1.2, circular arc ceiling).

Cross plots of the contour data along the red line shown in each image are presented in Figures 45 and 46 for the flat-wall and circular-arc wall cases, respectively. The position of this line relative to the PIV measurement plane and the model is shown in Figure 12. The displacement data are plotted versus the Y (cross-stream) coordinate of each measurement point. Because the interrogation grid was rotated 45° with respect to the tunnel axes to match the orientation of the model, the X (streamwise) coordinates of points along the measurement line are not constant (Fig. 12). The (X, Y) coordinates of the end-points of the cross-plot line were approximately (52, -47) and (-36, 41).

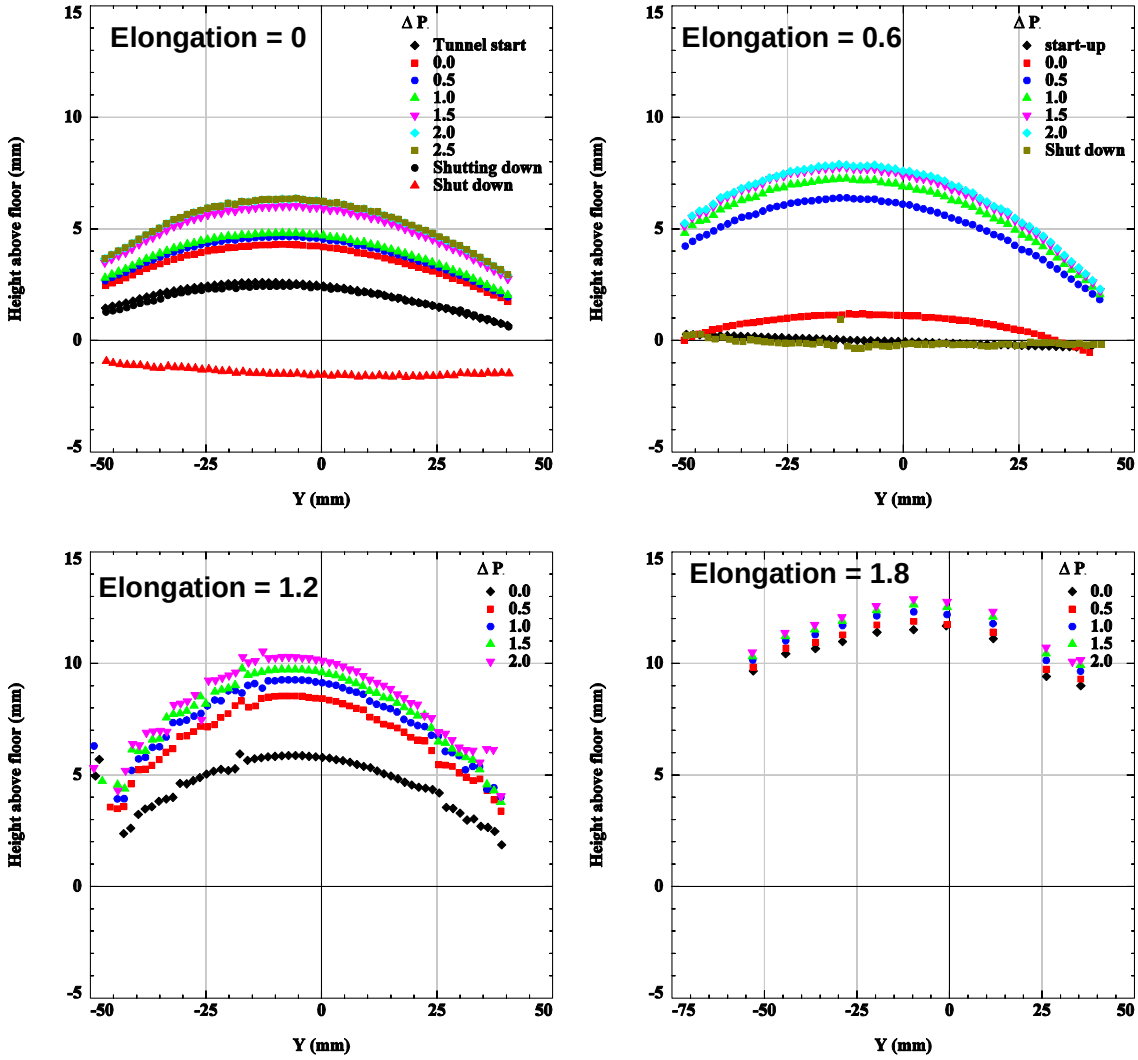

Figure 45. Cross-plots of out-of-plane displacements for different elongations and plenum pressures (Runs 21, 22, 23, 24, Kevlar model, flat ceiling).

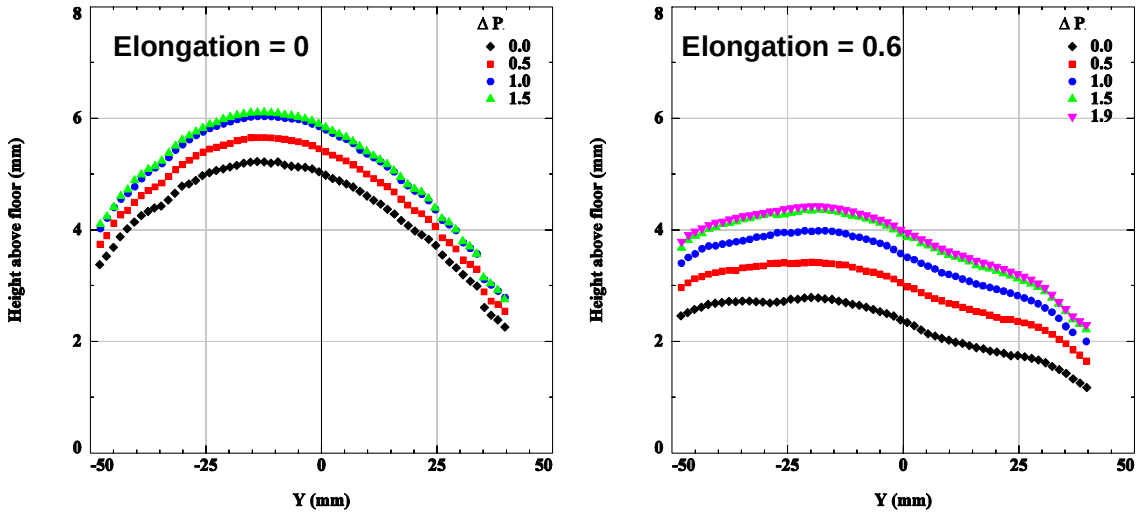

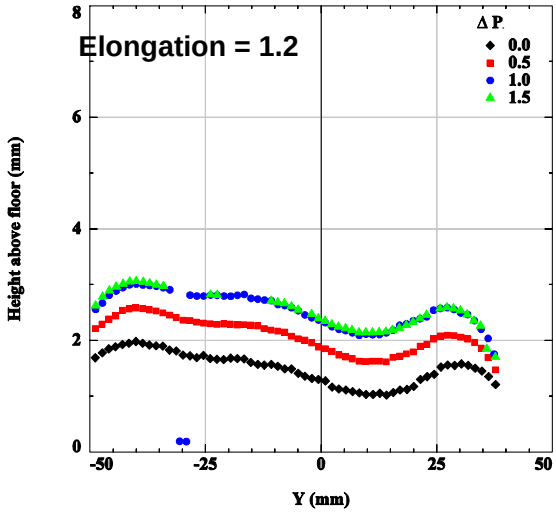

Figure 46. Cross-cuts of out-of-plane displacements for different elongations and plenum pressures (Runs 37 38, 39, Kevlar model, circular arc ceiling).

Figure 47 shows the effect of model elongation on out-of-plane displacement along the cross-cut line. The data are shown separately for each wall configuration (flat and circular arc) at ΔP = 1.5 psi. Note that the trend of displacement with elongation is reversed in the circular-arc case compared to the flat-wall case: displacement increases with elongation for the flat-wall cases, but decreases with elongation in the circular arc cases.

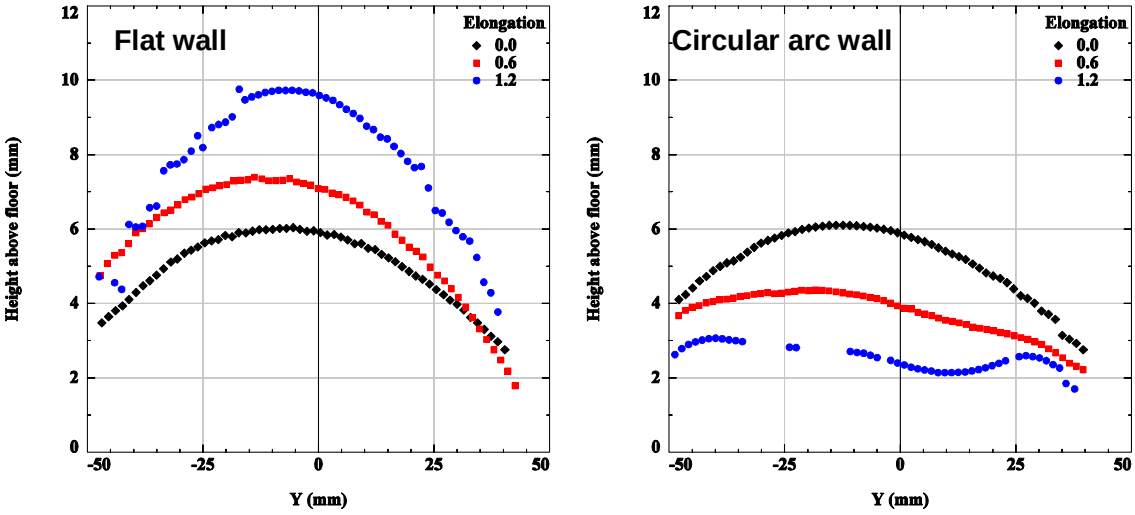

Figure 47. Effect of elongation on out-of-plane displacements (Kevlar model, ΔP = 1.5 psi).

Figure 48 directly compares the effect of the top-wall configuration on the model displacement for three model elongations. These data are also at ΔP = 1.5. Note that the relative magnitudes between the flat- and circular-arc wall cases are reversed for elongations 0.6 and 1.2 compared to elongation = 0.

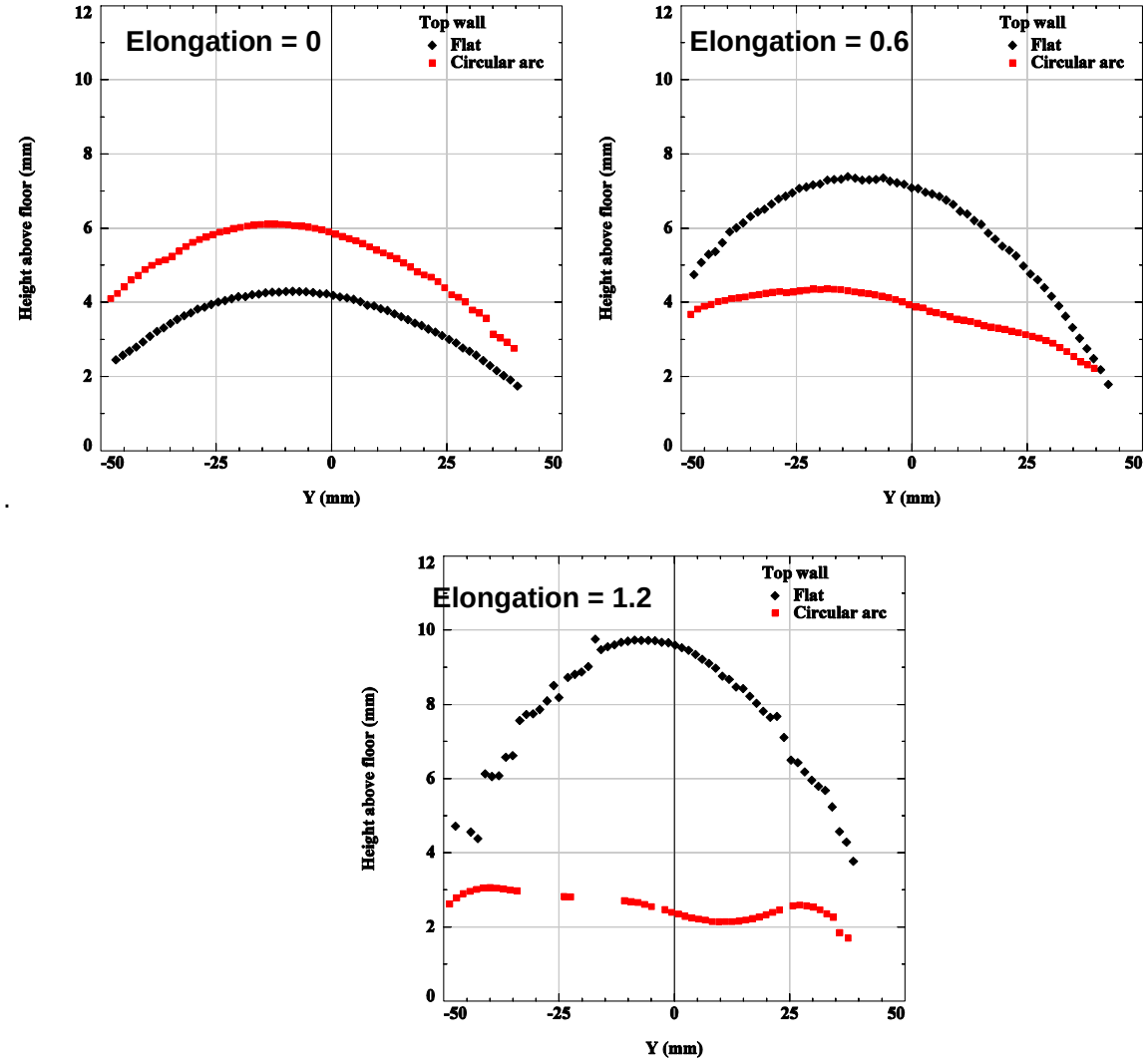

Figure 48. Effect of shape of top wall on out-of-plane displacements at different elongations (Kevlar model, ΔP = 1.5 psi).

The uncertainty in measuring the displacement points on the model was between 0.1 and 1 mm. Most of this uncertainty was due to uncertainty in establishing correspondence between measurement points in the images of the two cameras. Factors contributing to this uncertainty included: the large difference in perspective between the cameras due to their large convergence angle; the lack of reference images where the geometry of the model was known; the coarse weave of the model; directional lighting that created dark shadows when the model deformed out of plane and amplified the apparent texture of the model's weave; low contrast between the model surface and the random speckles and too few speckles; and occasional abrupt changes in the shape of the model.

A more robust algorithm is required to establish correspondence at large camera convergence angles when the initial approximate shape of the model is not known in advance. The convergence angle for this test (110°) was well beyond angles recommended when using commercial photogrammetry software (20-30°) that relies on digital image correlation to establish correspondence. Thus, one way to mitigate the correspondence problem is to reduce the camera convergence angle. However, this would come at the expense of lower sensitivity to out-of-plane

displacements. In the present test the camera separation, and thus convergence angle, was limited by the need to place the circular-arc insert between the cameras.

At conditions where the Kevlar models were elongated significantly in the stream-wise direction, at wind-off conditions the model surface was not planar but exhibited out-of-plane displacements that appeared as longitudinal channels (Fig. 49). As the stretching increased, the displacements increased and the channels became more pronounced. This presented several problems for the data-reduction procedure. Most importantly, for these highly elongated cases there were no images of the undeformed model that could be used to establish correspondence between nodes in images A and B. Although the channeling usually disappeared after the tunnel was started and there was a pressure difference across the fabric, the pressure caused the model to bulge outward so that it was not planar at this condition either (Fig. 50). A solution to this problem would be to image the model as it is being stretched, thus allowing correspondence to be established in the first images where the model was not stretched and when there were no channels. Then, in the remainder of the sequence, the grid would stretch with the model as it was deformed by virtue of the node-tracking procedure described above (note that these improvements were implemented during phase 2).

A second problem created by elongation was that, because the model was lit from the side, the bottoms of the channels were in shadow (Fig. 49). This made the speckles less visible and aggravated the problem of trying to establish correspondence of nodes. A solution to this problem is to provide non-directional lighting.

The Kevlar models exhibited a regular, very coarse weave (Figs. 49-50) that made data reduction more difficult. The weave appeared as a regular intensity pattern that resulted in cross-correlation functions with regularly spaced secondary peaks; the separation between peaks in both directions was the same as the “wavelength” of the weave. In addition to this pattern of secondary peaks, the correlation function included a peak associated with the displacement of the random speckles, which was what we wanted to measure. This peak was usually larger than all secondary peaks; however, when the contrast between the speckles and the fabric was low, as it was in shadows, the magnitude of this peak was only slightly greater than, or sometimes even less than, the secondary peaks. The side-lighting made the weave even more exaggerated and increased the magnitudes of the secondary peaks, making it that much more difficult to locate the primary peak.

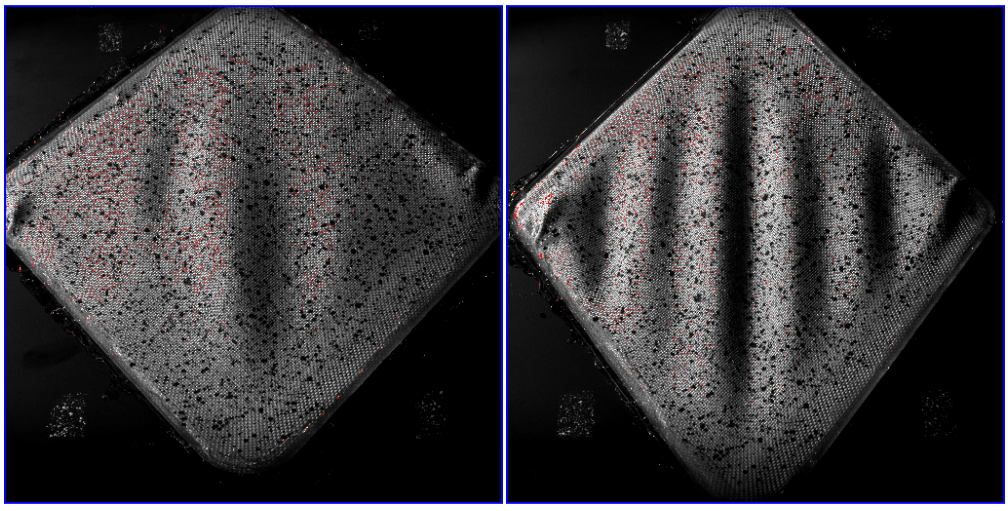

Figure 49. Wind-off image of Kevlar model at elongations 1.2 (Run 23) and 1.8 (Run 24) showing longitudinal channels.

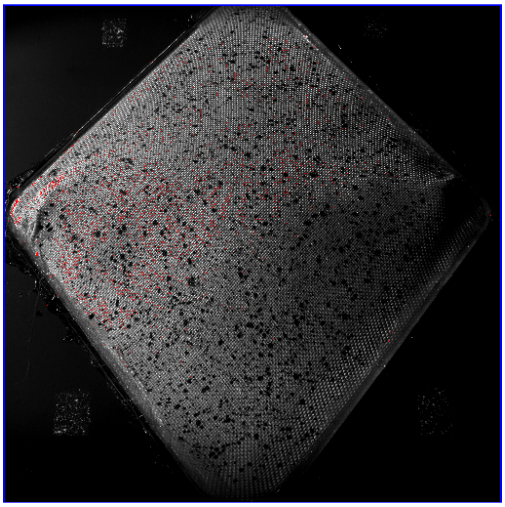

Figure 50. Wind-on image of model at maximum elongation with bulge due to pressure difference.

Phase 2 Tests

Several improvements were incorporated into the photogrammetry system for Phase two. As before, the cameras were mounted above the test section on the test section centerline, one upstream and one downstream of the test article. For phase two, no bump was employed on the inside surface of the upper wall because fabric buckling was achievable without the presence of the pressure gradient induced by the bump. This change made it possible to slightly increase the sizes of the windows through which the cameras viewed the test article. This also slightly reduced the angular separation between the cameras. Another important improvement was that the model was illuminated from above rather than from the side. This prevented shadows from being cast in the longitudinal furrows that formed when the test article was elongated. Another change was that the speckles on the fabric test article were smaller and denser than in phase one to allow better spatial resolution. The most important change was one of procedure: before images were acquired at wind-on conditions, the test article was imaged continuously as it was elongated at wind-off conditions. The interrogation grid was defined based on images acquired before the model was stretched, when the model was approximately square. At this undeformed condition it was easy to establish correspondence between nodes of the grid in the images of both cameras (that is, ensure that each node of the grid overlay the same physical point on the model in the images of both cameras). Then, as the model was stretched, the grid stretched with the model as if it were glued to it thereby preserving correspondence of all nodes even at maximum elongation when longitudinal furrows formed. This provided a good initial condition for the wind-on measurements and also allowed separating the model displacements that were due to stretching from those due to aerodynamic loading.

Figure 51 (left) shows the out-of plane displacements (delta z) of the test article at wind-off conditions and maximum elongation. Note the longitudinal furrows. Figure 51 (right) shows the additional out-of-plane displacements due to aerodynamic loads. Flow direction is bottom to top. All dimensions in mm. Figures 52 and 53 are similar comparisons of displacements in the in-plane streamwise (Fig 52) and cross-stream (Fig. 53) directions.

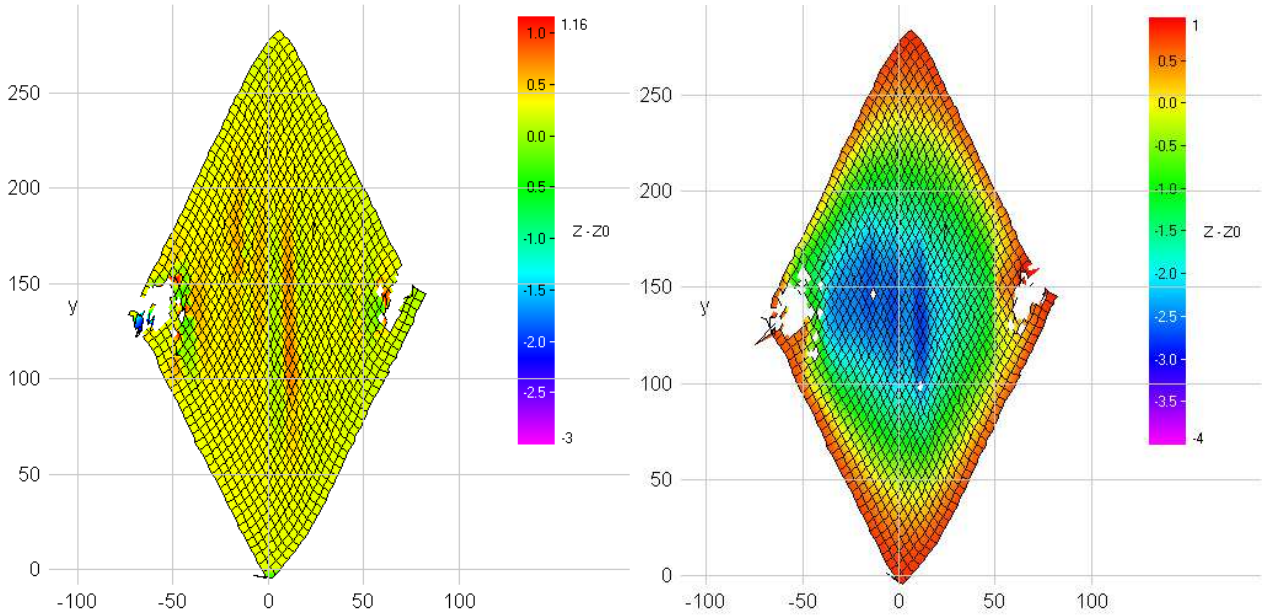

Figure 51. Out-of-plane displacements due to wind-off elongation (left) and aerodynamic loads (right).

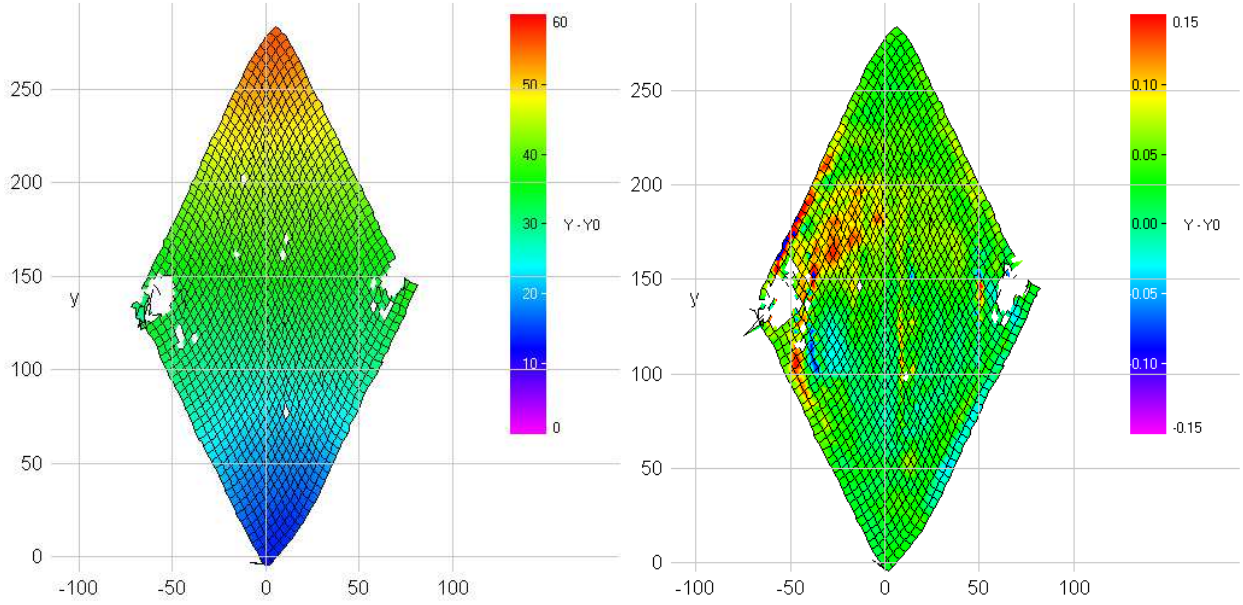

Figure 52. Streamwise displacements due to wind-off stretching (left) and aerodynamic loads (right).

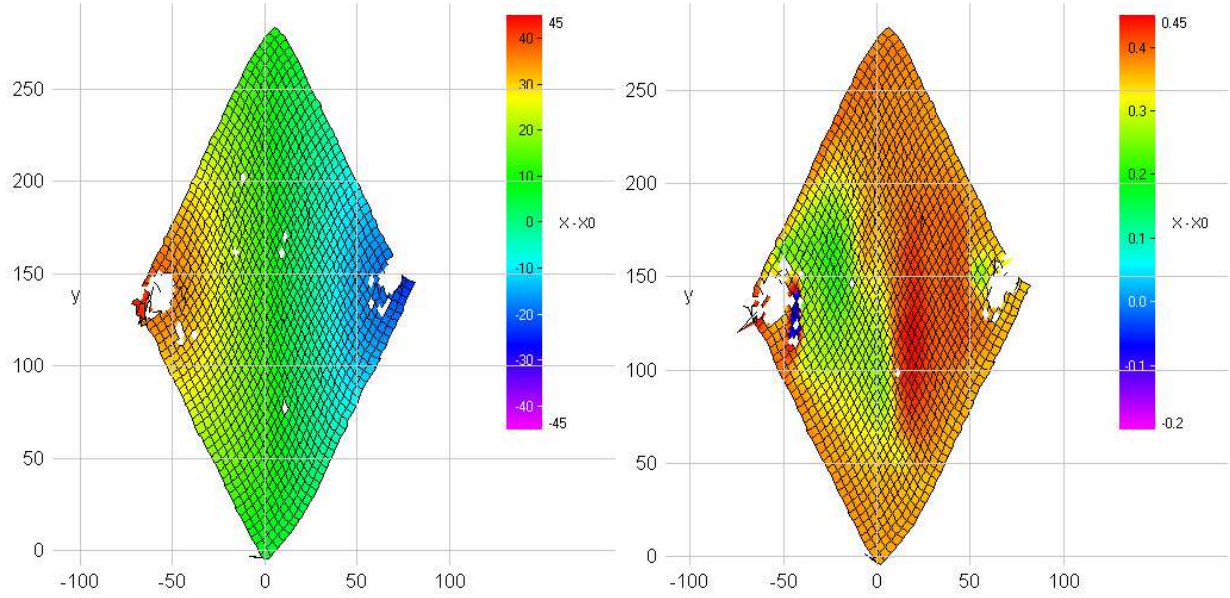

Figure 53. In-plane lateral displacements due to wind-off stretching (left) and aerodynamic loads (right).

Figure 54 (left) shows an image from the upstream camera with the grid overlaid. Figure 54 (right) shows out-of-plane displacements along the row of the grid indicated in Figure 54 (left). The red symbols show displacements due to stretching; the black symbols show displacements due to aerodynamic loads. Figure 55 shows model displacement data and PIV stream-wise velocity measurements. The PIV plane was vertical, 120 mm downstream of the upstream point of the test article.

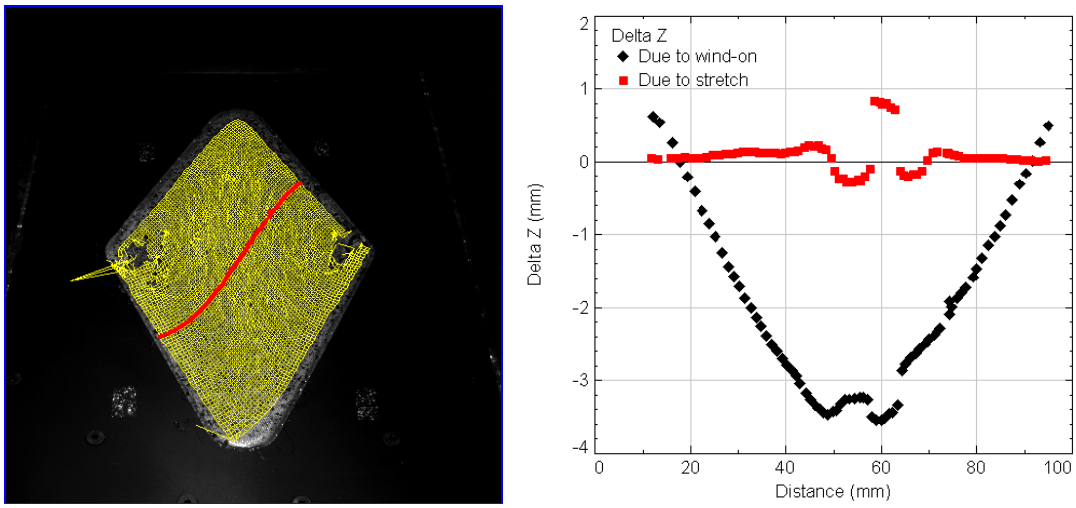

Figure 54. Image from upstream camera (left) and out-of-plane displacements (right) along row indicated by red dots.

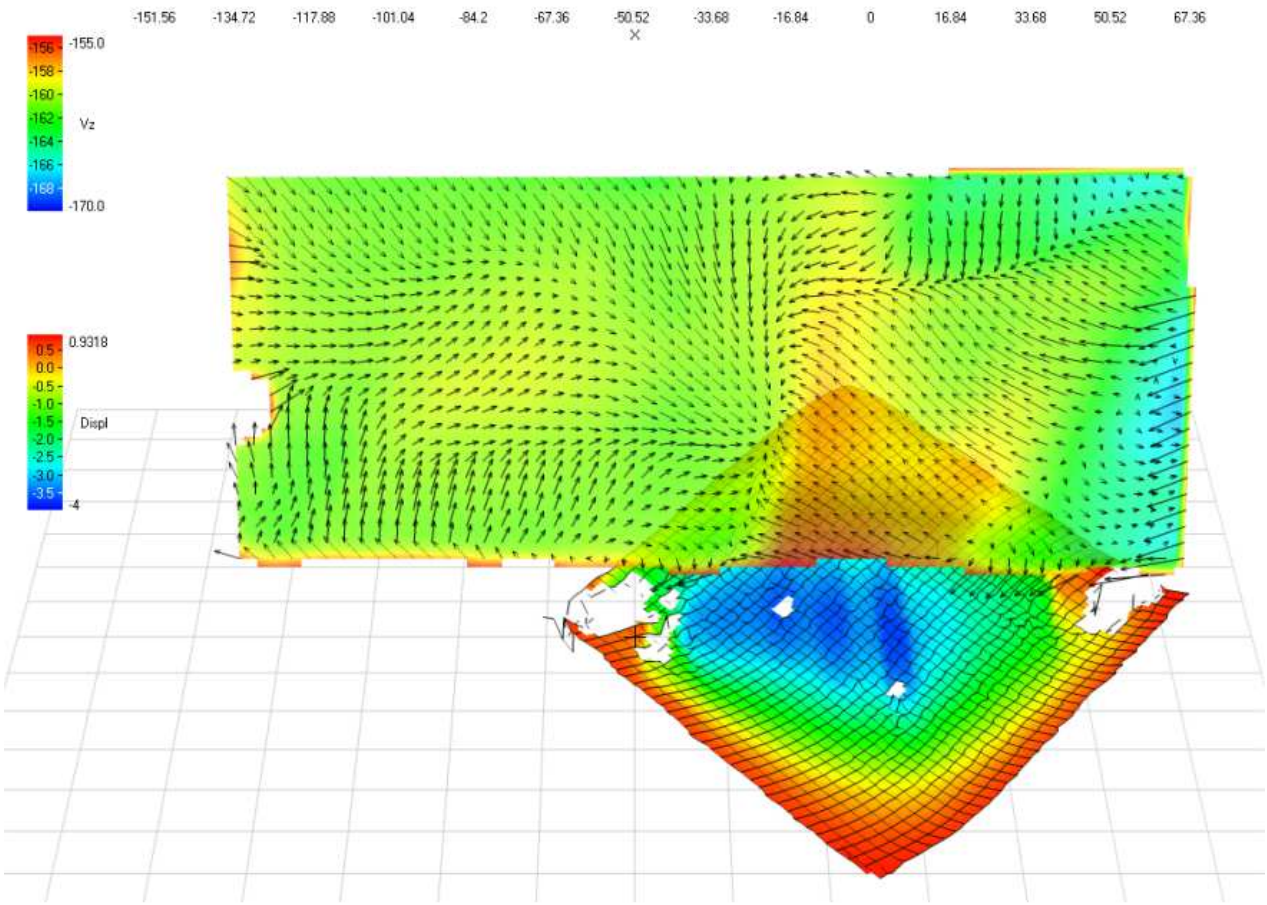

Figure 55. PIV and photogrammetry measurements. View is along tunnel axis looking downstream, Vinf = 566.8 ft/sec, ΔP = -0.08 psi, Elongation = 2.4 in, Kevlar Tension = 13 N/cm.

CONCLUSIONS

This document summarized the development of an experiment designed to provide data on fabrics suitable for validation of FSI computer codes. The apparatus developed for holding the fabric samples was geometrically simple with well defined boundary conditions yet permitted combined loads (structural and aerodynamic) to be applied in a controlled fashion. Although a substantial quantity of data was obtained during the wind tunnel tests, only a representative subset has been fully reduced and analyzed. It was found during testing that the phenomenon of greatest interest (i.e fabric buckling or wrinkling) that was present with the flow off did not persist once the flow was turned on. This was found to be the case even at low pressure differentials across the fabric. A follow-on experiment (i.e. phase 2 tests) was conducted wherein the test conditions were tailored in an attempt to achieve a flow-on buckled fabric state. Buckling was observed in this experiment at very low pressure differences across the tensioned fabric panel. Even though not all the test objectives were met, a dataset was produced that should be of interest to the FSI modeling community.

During this test, many areas of test technique improvement were identified. In particular, obtaining PIV measurements close to the fabric surface was found to be problematic. Other improvements include providing lighting of greater uniformity for the deformation measurements and tracking the fabric deformation using photogrammetry while the fabric is being elongated by the jack screw.

REFERENCES

1.) Rohrscheider, Ruben, “Variable-Fidelity Hypersonic Aeroelastic Analysis of Thin-Film Ballutes for Aerocapture,” Thesis Georgia Institute of Technology, May 2007.
2.) Lin, J. K., Shook, L. S., Ware, J. S., and Welch, J. V., “Flexible Thermal Protective System (TPS) Mechanical Testing Final Report,” ILC Dover, LP Frederica, DE, 2010.
3.) Blandino, J.R. Johnson, J.D. and Dharamsi, U.K., “Corner Wrinkling of a Square Membrane Due to Symmetric Mechanical Loads” JOURNAL OF SPACECRAFT AND ROCKETS, Vol. 39, No. 5, September–October 2002 p. 717-724.
4.) Leifer, J., Belvin, W. K., “Prediction of Wrinkle Amplitudes in Thin Film Membranes Using Finite Element Modeling,” AIAA 2003-1983, 44th AIAA/ASME/ASCE/AHS Structures, Structural Dynamics, and Materials Conference, 7-10 April 2003, Norfolk, Virginia 2003.
5.) Cao, J. et al., “Characterization of Mechanical Behavior of Woven Fabrics: Experimental Methods and Benchmark Results,” Composites: Part A (2008), doi:10.1016/ j.compositesa. 2008.02.016.
6.) Lebrun, G., Bureau, M. N. and Denault, J., “Evaluation of Bias-Extension and Picture-Frame Test Methods for the Measurement of Intraply Shear Properties of PP/Glass Commingled Fabrics,” Composite Structures 61, Elsevier Science Ltd., 2003, p. 341–352.
7.) Karara, H. M., and Abdel-Aziz, Y. I., “Accuracy Aspects of Non-Metric Imageries.” Photogrammetric Engineering, 40(7)1107–1117, 1974.
8.) Schairer, E.T., Heineck, J.T., Walker, L. A., Kushner, L.K., Zilliac, G.G., “Simultaneous, Unsteady PIV and Photogrammetry Measurements of a Tension-Cone Decelerator in Subsonic Flow,” presented at 15th International Symposium on Applications of Laser techniques to Fluid Mechanics, Lisbon, Portugal, July 5-8, 2010.
9.) Schairer, E.T. and Heineck, J.T., “Photogrammetric Recession Measurements of Ablative Materials in Arcjets,” Measurement Science and Technology, 21, 025304, 2010.

Appendix A – Selected Measured Data

A	B	E	G	I	K	L	M	N	O	P	Q	U
Run	Seq	Load	P_{plenum}	P_{static}	$P_{dynamic}$	delta p	Fabric	Direction	Initial Tension	Elongation	Insert	Comment
		lbs	psi	psi	psi	psi			N/cm	in		
1	2	12.96	-2.474	-2.460	2.297	-0.014	N	S	NM	0	NO	
1	3	13.79	-2.278	-2.457	2.293	0.180	N	S	NM	0	NO	
1	7	12.74	-2.476	-2.465	2.301	-0.011	N	S	NM	0.1	NO	
1	8	13.53	-2.274	-2.461	2.295	0.186	N	S	NM	0.1	NO	
3	3	12.50	-2.476	-2.467	2.297	-0.009	N	S	8.5	0.2	NO	
3	4	13.35	-2.276	-2.460	2.291	0.184	N	S	8.5	0.2	NO	
4	3	12.41	-2.483	-2.468	2.299	-0.015	N	S	8	0.6	NO	
4	4	12.48	-2.242	-2.463	2.294	0.221	N	S	8	0.6	NO	
4	5	12.53	-2.238	-2.462	2.293	0.225	N	S	8	0.6	NO	
4	6	12.50	-2.483	-2.468	2.298	-0.015	N	S	8	0.6	NO	
5	3	17.06	-2.428	-2.462	2.292	0.034	N	S	7.8	1.2	NO	
5	4	19.19	-1.926	-2.458	2.287	0.532	N	S	7.8	1.2	NO	
5	5	18.48	-1.945	-2.458	2.287	0.513	N	S	7.8	1.2	NO	
5	6	16.22	-2.436	-2.464	2.292	0.028	N	S	7.8	1.2	NO	
7	3	13.17	-2.485	-2.465	2.293	-0.020	N	T	12	0	NO	
7	4	14.01	-2.369	-2.459	2.286	0.090	N	T	12	0	NO	
8	3	23.58	-2.486	-2.466	2.292	-0.020	N	T	11	0.6	NO	
8	4	23.45	-2.380	-2.463	2.289	0.083	N	T	11	0.6	NO	
8	5	22.18	-2.489	-2.468	2.293	-0.021	N	T	11	0.6	NO	
12	2	21.77	-0.131	-2.470	2.297	2.339	K	S	15	0	NO	PIV setup was incorrect; re-run later to sync tunnel and PIV data
12	3	11.72	-2.376	-2.467	2.292	0.091	K	S	15	0	NO	PIV data fault
12	4	13.69	-1.923	-2.470	2.292	0.547	K	S	15	0	NO	PIV data fault
12	5	16.00	-1.390	-2.471	2.291	1.081	K	S	15	0	NO	PIV data fault
12	6	17.85	-1.022	-2.471	2.290	1.449	K	S	15	0	NO	PIV data fault
12	7	19.93	-0.489	-2.472	2.289	1.983	K	S	15	0	NO	PIV data fault
12	8	19.51	-0.145	-2.473	2.288	2.328	K	S	15	0	NO	PIV data fault
13	2	17.61	-2.230	-2.488	2.306	0.257	K	S	12	0.1	NO	PIV data fault; tape came up and tripped BL; redo in Run 14
13	3	20.34	-2.009	-2.488	2.305	0.478	K	S	12	0.1	NO	PIV data fault; tape came up and tripped BL; redo in Run 14
13	4	23.75	-1.375	-2.486	2.302	1.110	K	S	12	0.1	NO	PIV data fault; tape came up and tripped BL; redo in Run 14
13	5	24.82	-1.077	-2.486	2.302	1.409	K	S	12	0.1	NO	PIV data fault; tape came up and tripped BL; redo in Run 14
13	6	27.81	-0.558	-2.486	2.302	1.928	K	S	12	0.1	NO	PIV data fault; tape came up and tripped BL; redo in Run 14
14	2	16.65	-2.576	-2.490	2.307	-0.087	K	S	12	0.1	NO	PIV data fault; repeat of Run 13
14	3	20.97	-2.065	-2.493	2.307	0.428	K	S	12	0.1	NO	PIV data fault; repeat of Run 13
14	4	23.69	-1.477	-2.493	2.306	1.015	K	S	12	0.1	NO	PIV data fault; repeat of Run 13
14	5	24.65	-1.087	-2.493	2.306	1.406	K	S	12	0.1	NO	PIV data fault; repeat of Run 13
14	6	28.96	-0.421	-2.494	2.306	2.073	K	S	12	0.1	NO	PIV data fault; repeat of Run 13
14	7	29.88	-0.165	-2.493	2.304	2.328	K	S	12	0.1	NO	PIV data fault; repeat of Run 13
15	2	24.97	-2.315	-2.489	2.303	0.174	K	S	NM	0.2	NO	PIV data fault
15	3	27.20	-2.009	-2.491	2.304	0.482	K	S	NM	0.2	NO	PIV data fault
15	4	30.24	-1.529	-2.490	2.302	0.961	K	S	NM	0.2	NO	PIV data fault
15	5	33.57	-1.057	-2.490	2.301	1.433	K	S	NM	0.2	NO	PIV data fault
15	6	36.40	-0.504	-2.490	2.301	1.986	K	S	NM	0.2	NO	PIV data fault
15	7	38.95	-0.107	-2.490	2.300	2.384	K	S	NM	0.2	NO	PIV data fault

A	B	E	G	I	K	L	M	N	O	P	Q	U
Run	Seq	Load	P_{plenum}	P_{static}	$P_{dynamic}$	delta P	Fabric	Direction	Initial Tension	Elongation	Insert	Comment
16	3	74.58	-2.392	-2.492	2.303	0.100	K	S	130	0.6	NO	PIV data fault
16	4	77.76	-1.932	-2.492	2.303	0.560	K	S	130	0.6	NO	PIV data fault
16	5	80.51	-1.524	-2.493	2.302	0.968	K	S	130	0.6	NO	PIV data fault
16	6	85.54	-1.026	-2.493	2.302	1.467	K	S	130	0.6	NO	PIV data fault
16	7	91.39	-0.481	-2.494	2.303	2.014	K	S	130	0.6	NO	PIV data fault
16	8	96.67	-0.094	-2.494	2.302	2.400	K	S	130	0.6	NO	PIV data fault
17	2	13.33	-2.537	-2.495	2.303	-0.042	K	S	15	0.1	NO	PIV data fault; repeat of Run 14
17	3	13.89	-2.079	-2.496	2.303	0.418	K	S	15	0.1	NO	PIV data fault; repeat of Run 14
17	4	17.14	-1.505	-2.496	2.302	0.991	K	S	15	0.1	NO	PIV data fault; repeat of Run 14
17	5	19.26	-1.039	-2.496	2.301	1.457	K	S	15	0.1	NO	PIV data fault; repeat of Run 14
17	6	20.19	-0.530	-2.496	2.301	1.966	K	S	15	0.1	NO	PIV data fault; repeat of Run 14
17	7	19.28	-0.549	-2.496	2.301	1.947	K	S	15	0.1	NO	PIV data fault; repeat of Run 14
18	2	16.40	-1.896	-2.515	2.321	0.618	K	T	11	0	NO	PIV data fault
18	3	16.31	-1.920	-2.515	2.321	0.595	K	T	11	0	NO	PIV data fault
18	4	16.26	-1.531	-2.515	2.320	0.984	K	T	11	0	NO	PIV data fault
18	5	16.38	-1.105	-2.516	2.320	1.411	K	T	11	0	NO	PIV data fault
18	6	15.54	-0.566	-2.516	2.320	1.950	K	T	11	0	NO	PIV data fault
18	7	15.21	-0.031	-2.516	2.319	2.485	K	T	11	0	NO	PIV data fault; K ripped during setup of run 19
20	3	N/A	-0.014	-2.517	2.319	2.503	-	-	N/A	N/A	NO	Empty Tunnel Run to test corrected PIV setup
21	2	14.34	-2.502	-2.513	2.317	0.011	K	S	10	0	NO	Repeat of Run 12 with corrected PIV setup
21	3	14.50	-1.998	-2.513	2.315	0.515	K	S	10	0	NO	Repeat of Run 12 with corrected PIV setup
21	4	14.52	-1.511	-2.513	2.314	1.002	K	S	10	0	NO	Repeat of Run 12 with corrected PIV setup
21	5	14.55	-1.052	-2.514	2.314	1.462	K	S	10	0	NO	Repeat of Run 12 with corrected PIV setup
21	6	14.61	-0.523	-2.514	2.313	1.990	K	S	10	0	NO	Repeat of Run 12 with corrected PIV setup
21	7	14.52	-0.098	-2.514	2.313	2.416	K	S	10	0	NO	Repeat of Run 12 with corrected PIV setup
22	3	27.34	-2.535	-2.506	2.307	-0.028	K	S	8	0.6	NO	Repeat of Run 16 with corrected PIV setup
22	4	27.53	-2.055	-2.506	2.305	0.452	K	S	8	0.6	NO	Repeat of Run 16 with corrected PIV setup
22	5	27.64	-1.515	-2.507	2.304	0.992	K	S	8	0.6	NO	Repeat of Run 16 with corrected PIV setup
22	6	26.67	-1.059	-2.506	2.303	1.447	K	S	8	0.6	NO	Repeat of Run 16 with corrected PIV setup
23	3	66.56	-2.455	-2.468	2.267	0.013	K	S	OS	1.2	NO	
23	4	67.27	-2.012	-2.469	2.267	0.457	K	S	OS	1.2	NO	
23	5	65.27	-1.509	-2.469	2.267	0.960	K	S	OS	1.2	NO	
23	6	64.68	-1.077	-2.469	2.267	1.392	K	S	OS	1.2	NO	
23	7	62.35	-0.499	-2.469	2.266	1.970	K	S	OS	1.2	NO	
24	3	61.26	-2.471	-2.468	2.265	-0.003	K	S	OS	1.8	NO	
24	4	58.67	-1.988	-2.469	2.265	0.481	K	S	OS	1.8	NO	
24	5	55.61	-1.478	-2.469	2.265	0.992	K	S	OS	1.8	NO	
24	6	53.50	-0.997	-2.469	2.265	1.472	K	S	OS	1.8	NO	
24	7	54.36	-2.142	-2.469	2.265	0.327	K	S	OS	1.8	NO	
25	2	32.74	-2.365	-2.408	2.207	0.043	K	S	OS	2.4	NO	

	A	B	E	G	I	K	L	M	N	O	P	Q	U
1	Run	Seq	Load	p_{plenum}	p_{static}	$p_{dynamic}$	delta p	Fabric	Direction	Initial Tension	Elongation	Insert	Comment
106	25	3	31.99	-1.837	-2.409	2.207	0.572	K	S	OS	2.4	NO	
107	25	4	30.85	-1.395	-2.409	2.207	1.014	K	S	OS	2.4	NO	
108	25	5	32.11	-0.900	-2.410	2.207	1.510	K	S	OS	2.4	NO	
109	25	6	31.92	-0.393	-2.411	2.206	2.017	K	S	OS	2.4	NO	
110	25	7	32.70	-0.160	-2.411	2.206	2.250	K	S	OS	2.4	NO	
112	26	2	15.70	-2.370	-2.361	2.164	-0.009	K	T	13	0	NO	Repeat of Run 18 with corrected PIV setup
113	26	3	17.49	-1.848	-2.362	2.163	0.514	K	T	13	0	NO	Repeat of Run 18 with corrected PIV setup
114	26	4	18.57	-1.341	-2.363	2.164	1.022	K	T	13	0	NO	Repeat of Run 18 with corrected PIV setup
115	26	5	19.59	-0.846	-2.363	2.162	1.517	K	T	13	0	NO	Repeat of Run 18 with corrected PIV setup
116	26	6	19.79	-0.361	-2.364	2.162	2.003	K	T	13	0	NO	Repeat of Run 18 with corrected PIV setup
117	26	7	19.78	-0.081	-2.365	2.163	2.284	K	T	13	0	NO	Repeat of Run 18 with corrected PIV setup
119	27	2	53.80	-2.312	-2.323	2.122	0.012	K	T	28.5	0.1	NO	
120	27	3	57.35	-1.852	-2.323	2.122	0.471	K	T	28.5	0.1	NO	
121	27	4	62.56	-1.342	-2.326	2.123	0.983	K	T	28.5	0.1	NO	
122	27	5	67.68	-0.836	-2.326	2.122	1.489	K	T	28.5	0.1	NO	
123	27	6	72.61	-0.323	-2.325	2.121	2.002	K	T	28.5	0.1	NO	
124	27	7	74.67	-0.092	-2.326	2.122	2.234	K	T	28.5	0.1	NO	
127	28	3	180.66	-2.274	-2.291	2.090	0.018	K	T	70	0.2	NO	
128	28	4	184.10	-1.778	-2.291	2.090	0.513	K	T	70	0.2	NO	
129	28	5	187.68	-1.283	-2.292	2.090	1.008	K	T	70	0.2	NO	
130	28	6	192.02	-0.784	-2.292	2.089	1.508	K	T	70	0.2	NO	
131	28	7	195.86	-0.282	-2.292	2.089	2.010	K	T	70	0.2	NO	
133	29	3	N/A	-0.025	-2.288	2.087	2.263	N/A	N/A	N/A	N/A	NO	Empty tunnel run to install and test the aerodynamic insert
135	30	3	45.72	-2.720	-2.280	2.076	-0.441	N	S	8	0	YES	
137	31	3	33.13	-3.026	-2.285	2.079	-0.741	N	S	7.5	0.6	YES	
139	32	3	36.50	-3.015	-2.284	2.078	-0.731	N	T	7	0	YES	
140	32	4	41.40	-2.736	-2.281	2.074	-0.455	N	T	7	0	YES	
142	33	3	22.14	-3.033	-2.284	2.075	-0.749	N	T	7	0.1	YES	
144	34	3	41.31	-3.041	-2.285	2.074	-0.757	N	T	OS	0.2	YES	
145	34	4	44.29	-2.753	-2.280	2.069	-0.473	N	T	OS	0.2	YES	
147	36	3	21.76	-2.176	-2.200	1.993	0.025	K	S	17.8	0	YES	PIV issue arose
148	36	4	21.88	-2.172	-2.200	1.993	0.028	K	S	17.8	0	YES	PIV issue arose
149	36	5	23.00	-1.681	-2.199	1.991	0.518	K	S	17.8	0	YES	PIV issue arose
150	36	6	22.62	-1.181	-2.199	1.991	1.018	K	S	17.8	0	YES	PIV issue arose
151	36	7	23.93	-0.680	-2.199	1.991	1.519	K	S	17.8	0	YES	PIV issue arose
153	37	3	25.60	-2.153	-2.168	1.962	0.015	K	S	11	0	YES	Re-run of Run 36; PIV issue corrected
154	37	4	26.76	-1.656	-2.169	1.963	0.513	K	S	11	0	YES	Re-run of Run 36; PIV issue corrected
155	37	5	25.53	-1.673	-2.169	1.962	0.497	K	S	11	0	YES	Re-run of Run 36; PIV issue corrected
156	37	6	26.87	-1.140	-2.168	1.961	1.028	K	S	11	0	YES	Re-run of Run 36; PIV issue corrected

Run	Seq	Load	ρ_{plenum}	ρ_{static}	$\rho_{dynamic}$	delta ρ	Fabric	Direction	Initial Tension	Elongation	Insert	Comment
38	3	46.81	-2.102	-2.133	1.928	0.032	K	S	60	0.6	YES	
38	4	48.66	-1.621	-2.133	1.927	0.512	K	S	60	0.6	YES	
38	5	51.69	-1.116	-2.132	1.927	1.017	K	S	60	0.6	YES	
38	6	54.62	-0.625	-2.132	1.926	1.507	K	S	60	0.6	YES	
39	3	78.66	-2.076	-2.105	1.900	0.029	K	S	65	1.2	YES	Fabric slipped during run; data could be compromised
39	4	80.57	-1.588	-2.104	1.899	0.516	K	S	65	1.2	YES	Fabric slipped during run; data could be compromised
39	5	84.57	-1.106	-2.104	1.899	0.998	K	S	65	1.2	YES	Fabric slipped during run; data could be compromised
39	6	87.31	-0.595	-2.104	1.898	1.509	K	S	65	1.2	YES	Fabric slipped during run; data could be compromised
40	3	17.26	-2.032	-2.097	1.897	0.065	K	T	10	0	YES	
40	4	17.43	-1.588	-2.097	1.897	0.509	K	T	10	0	YES	
40	5	17.84	-1.097	-2.098	1.897	1.000	K	T	10	0	YES	
40	6	18.66	-0.869	-2.097	1.896	1.229	K	T	10	0	YES	
41	3	38.42	-2.052	-2.096	1.895	0.045	K	T	22	0.1	YES	
41	4	42.61	-1.571	-2.096	1.894	0.526	K	T	22	0.1	YES	
41	5	47.78	-1.090	-2.097	1.895	1.007	K	T	22	0.1	YES	
41	6	53.78	-0.557	-2.096	1.894	1.539	K	T	22	0.1	YES	
42	3	139.02	-2.056	-2.094	1.891	0.039	K	T	50	0.2	YES	
42	4	142.80	-1.564	-2.095	1.891	0.531	K	T	50	0.2	YES	
42	5	146.64	-1.091	-2.095	1.891	1.004	K	T	50	0.2	YES	
42	6	153.58	-0.579	-2.095	1.890	1.516	K	T	50	0.2	YES	

Nomenclature:	
	N: F-111 Un-coated Nylon 30 denier, 126x132 ypi 45 lb/in (warp x fill), min. 1.2 oz/yd^2; 3 mils
	K: ST11-4600 Silicone Coated Kevlar 840 denier, 26x26 ypi 650 lb/in (warp x fill), min. 10.2 oz/yd^2; 14 mils
	S: Shear direction (weave at 45 deg to flow)
	T: Tension direction (weave at 0 and 90 deg to flow)
	NM: not measured
	OS: off the scale (above or below - loose or wrinkled fabric)

REPORT DOCUMENTATION PAGE

Form Approved
OMB No. 0704-0188

1. REPORT DATE *(DD-MM-YYYY)*	2. REPORT TYPE	3. DATES COVERED *(From - To)*
28-09-2012	Technical Memorandum	October 2010 to September 2012

4. TITLE AND SUBTITLE

Development of a Fluid Structures Interaction Test Technique for Fabrics

5a. CONTRACT NUMBER

5b. GRANT NUMBER

5c. PROGRAM ELEMENT NUMBER

6. AUTHOR(S)

Gregory G. Zilliac
James T. Heineck
Edward T. Schairer
Robert N. Mosher
Theodore J. Garbeff
Louise A. Walker

5d. PROJECT NUMBER

5e. TASK NUMBER

5f. WORK UNIT NUMBER

7. PERFORMING ORGANIZATION NAME(S) AND ADDRESS(ES)

Ames Research Center
Moffett Field, CA 94035-1000

8. PERFORMING ORGANIZATION REPORT NUMBER

NASA/TM-2012-216052

9. SPONSORING/MONITORING AGENCY NAME(S) AND ADDRESS(ES)

National Aeronautics and Space Administration
Washington, DC 20546-0001

10. SPONSORING/MONITOR'S ACRONYM(S)

11. SPONSORING/MONITORING REPORT NUMBER

12. DISTRIBUTION/AVAILABILITY STATEMENT

Unclassified -- Unlimited
Subject Category 35 Distribution: Standard
Availability: NASA CASI (301) 621-0390

13. SUPPLEMENTARY NOTES

14. ABSTRACT

Application of fluid structures interaction (FSI) computational techniques to configurations of interest to the entry, descent and landing (EDL) community is limited by two factors – limited characterization of the material properties for fabrics of interest and insufficient experimental data to validate the FSI codes. Recently ILC Dover Inc. performed standard tests to characterize the static stress-strain response of four candidate fabrics for use in EDL applications. The objective of the tests described here is to address the need for a FSI dataset for CFD validation purposes. To reach this objective, the structural response of fabrics was measured in a very simple aerodynamic environment with well controlled boundary conditions. Two test series were undertaken. The first series covered a range of tunnel conditions and the second focused on conditions that resulted in fabric panel buckling.

15. SUBJECT TERMS

Aeronautics
Computational Fluid Dynamics
Descent

16. SECURITY CLASSIFICATION OF:			17. LIMITATION OF ABSTRACT	18. NUMBER OF PAGES	19b. NAME OF RESPONSIBLE PERSON
a. REPORT	b. ABSTRACT	c. THIS PAGE			Gregory Zilliac
U	U	U	UU	51	19b. TELEPHONE NUMBER *(Include area code)* (650) 604-3904